Dissimilar Control of Momentum and Heat Transfer in a Fully Developed Turbulent Channel Flow

Y. HASEGAWA[1,2] **AND N. KASAGI**[1]

[1]Department of Mechanical Engineering, The University of Tokyo, 7-3-1 Bunkyo-ku, Hongo, Tokyo 113-8656, Japan

[2]Center of Smart Interfaces, TU Darmstadt, Petersenstr. 32, 64287, Darmstadt, Germany

(Received 26 September 2011)

A wide range of applicability of the Reynolds analogy between turbulent momentum and heat transport implies inherent difficulty in diminishing or enhancing skin friction and heat transfer independently. In the present study, we introduce the suboptimal control theory for achieving a dissimilar control of enhancing heat transfer, while keeping the skin friction not increased considerably in a fully developed channel flow. The Fréchet differentials clearly show that the responses of velocity and temperature fields to wall blowing/suction are quite different due to the fact that the velocity is a divergence-free vector while the temperature is a conservative scalar. This essential difference allows us to achieve dissimilar control even in flows where the averaged momentum and energy transport equations have the identical form. It is also found that the resultant optimized mode of control input exhibits a streamwise traveling wave-like property. By exploring the phase relationship between the traveling wave-like control input and the velocity and thermal fields, we reveal that such control input contributes to dissimilar heat transfer enhancement via two different mechanisms, i.e., direct modification of the coherent components of the Reynolds shear stress and the turbulent heat flux, and indirect effects on the incoherent components through modification of the mean velocity and temperature profiles. Based on these results, a simple open-loop strategy for dissimilar control is proposed and assessed.

1. Introduction

Facing the global issues such as depletion of energy resources and environmental deterioration, highly efficient thermal-fluids systems are ever more required. Enhancement of heat and mass transfer processes in various systems such as heat exchangers, gas absorbers and chemical reactors should be extremely important for not only energy utilization, but also economy and the environment. In the meanwhile, wall skin friction, which necessitates pumping power to drive a working fluid, always needs to be suppressed, since the applied power is eventually dissipated by the fluid viscosity, and therefore results in the energy consumption. However, such dissimilar heat transfer enhancement should be a difficult task due to the similarity between the governing equations for the streamwise velocity component and the temperature in most of the shear flows.

Reynolds (1874) pioneered the analogy concept between turbulent momentum and heat transfer based on the mixing length theory. When the Prandtl number $\mathrm{Pr} = \nu^*/\alpha^*$ equal to unity, where ν^* and α^* are the kinematic viscosity and the thermal diffusivity of a fluid, respectively, the Reynolds analogy results in the following relationship between the

friction coefficient C_f and the Stanton number St:

$$2\mathrm{St} = C_f. \tag{1.1}$$

The above dimensionless parameters of C_f and St are defined as

$$C_f = \frac{\tau_w^*}{\frac{1}{2}\rho U_b^{*2}}, \tag{1.2}$$

$$\mathrm{St} = \frac{q_w^*}{\rho^* C_p^* U_b^* \Theta_b^*}, \tag{1.3}$$

where τ_w^* and q_w^* are the wall friction and the wall heat flux, while U_b^*, Θ_b^*, ρ^* and C_p^* are the bulk velocity, the bulk temperature, the fluid density and the thermal capacity of fluid, respectively. A quantity with an asterisk represents a dimensional value throughout the paper. By taking into account the effect of the Prandtl number, Chilton & Colburn (1934) modified Eq. (1.1) as $2\mathrm{St} = C_f \mathrm{Pr}^{-2/3}$, which is the most successful and widely used concept for predicting heat and mass transport in practical flows (see, e.g., Keys et al. 2005).

Mathematically, the streamwise velocity component and the temperature should have exactly the same solution, if their governing equations, boundary conditions and initial conditions are all identical. In practical flows, however, this is not the case. For example, the Prandtl number is not always unity, so that the diffusion effect appears differently in the momentum and energy transport equations. In a fully developed channel flow, the fluid is driven by a mean pressure gradient, which is uniform throughout the channel, whereas a heat source, if it exists, may change in time and space due to chemical reaction, viscous dissipation and so forth. A no-slip condition is generally assumed at the wall, while there exist a variety of thermal boundary conditions dependent on the conjugate heat transfer coupled with heat conduction inside wall (see, Kasagi et al. 1989). In view of these factors causing dissimilarity in momentum and heat transport, it is rather surprising that such a simple analogy concept holds well in a wide range of turbulent heat transfer problems.

Recently, Kasagi et al. (2011) summarized possible scenarios of dissimilar control by reexamining the governing equations and the boundary conditions for convective heat transfer. They categorize the basic strategies for achieving dissimilarity in turbulent flow into two groups, i.e., one based on the averaged quantities and the other based on the fluctuating turbulent components. In the former, it can be mathematically shown that the dissimilarity between the averaged momentum and heat transport equations causes a difference between local turbulence contributions to wall friction and wall heat flux. Such mathematical relationships are found to be useful to develop an algorithm for dissimilar control when the averaged momentum and heat transport equations have different forms.

When the averaged transport equations and the boundary conditions become similar, dissimilarity between momentum and heat transfer can be caused only by dissimilarity in turbulent transport mechanisms, i.e., dissimilarity between the Reynolds shear stress and the turbulent heat flux. In such cases, dissimilar control becomes even more difficult to achieve than in other cases. However, the dissimilar control is still possible, since there exists an essential difference between the vector and scalar quantities as shown below.

In order to examine the above argument, we revisit the transport equation of the velocity fluctuation u_i' given as:

$$\frac{\partial u_i'}{\partial t} + \overline{u_j}\frac{\partial u_i'}{\partial x_j} = -u_j'\frac{\partial \overline{u_i}}{\partial x_j} - \frac{\partial (u_i'u_j' - \overline{u_i'u_j'})}{\partial x_j} - \frac{\partial p}{\partial x_i} + \frac{1}{\mathrm{Re}}\frac{\partial u_i'}{\partial x_j \partial x_j}, \tag{1.4}$$

where an over-bar denotes averaging in homogeneous directions, while a prime a fluctuating quantity. When $\mathrm{Pr} = 1$, the transport equation for the temperature fluctuation θ' can be obtained by replacing u_i' with θ' in Eq. (1.4), but without the third term on the right-hand-side, i.e., the pressure gradient term. In an incompressible fluid, the pressure fluctuation instantaneously responds to the fluctuating velocity field so as to project it to the divergence-free space. Therefore, the three components of a velocity vector are coupled through the pressure term. On the other hand, a passive scalar quantity does not have such restriction. This fundamental difference between the velocity and scalar quantities should affect their dynamics, and therefore results in dissimilarity between the Reynolds shear stress and the turbulent heat flux in some cases. For example, Antonia & Krishnamoorthy (1988) made simultaneous measurement of the streamwise velocity fluctuation u' and the temperature fluctuation θ' in a turbulent boundary layer. They confirmed that the correlation between u' and θ' is deteriorated with increasing the distance from the wall, while it is kept high in the near-wall region. They also observed decrease in the spectral coherence between u' and θ' at high frequencies.

One may expect that the above insight provides more universal strategies for dissimilar control. Although various successful control strategies have been proposed for turbulent skin friction drag reduction in the last several decades (see, e.g., Kasagi et al. 2009, for review), only a few studies have been made on dissimilar heat transfer control exploiting the essential difference between a divergence-free vector and a conservative scalar. Suzuki et al. (1988) studied turbulent heat transfer in a flat plate boundary layer disturbed by an inserted cylinder. They heated both the flat plate and the cylinder so as to make the velocity and thermal boundary conditions similar. As a result, they still observed strong dissimilarity between momentum and heat transfer associated with intensification of the cold wallward and hot outward interaction modes behind the cylinder. Such phenomena should be caused by a streamwise pressure gradient induced by the cylinder, although they did not discuss the origin of the dissimilarity. Kong et al. (2001) reported significant local dissimilarity between C_f and St in the thermal boundary layer with slot blowing/suction through direct numerical simulation (DNS). They clearly showed that the streamwise pressure gradient induced by wall blowing/suction is the primary cause for dissimilarity.

Although these previous studies demonstrated a possibility of local dissimilar control, it has not been achieved in a fully developed turbulent channel flow. An attempt for such dissimilar control was once made by Yokoo et al. (2000) in a turbulent channel flow with isothermal two walls kept at different temperatures at a low Reynolds number. They defined a cost function including the variances of skin friction, wall heat flux, and velocity and temperature fluctuations with their weights, and applied the optimal control procedure (Bewley et al. 2001) in order to determine the control input, i.e., local blowing/suction so that the cost function is minimized. Despite the huge computational cost required for the optimization, the effect of control they have found remains very small. Clearly, a different approach with less computational load is desirable.

The objective of the present study is to establish a strategy for dissimilar heat transfer enhancement based on the essential difference between divergence-free vector and conservative scalar quantities. We consider one of the most canonical thermo-fluid systems, namely, fluid flow with heat transfer in a straight and smooth channel. The fluid properties are assumed constant and the temperature is a passive scalar so that any buoyancy effect does not arise. The molecular Prandtl number is set to be unity and uniform heat generation within the flow domain is assumed so that the averaged momentum and heat transport equations have exactly the same form. Such an ideal flow condition offers a chance to investigate dissimilarity caused only by the continuity constraint on the velocity field, while the other sources of dissimilarity are removed. In order to derive a control algorithm, we employ the so-called suboptimal control theory, which has been success-

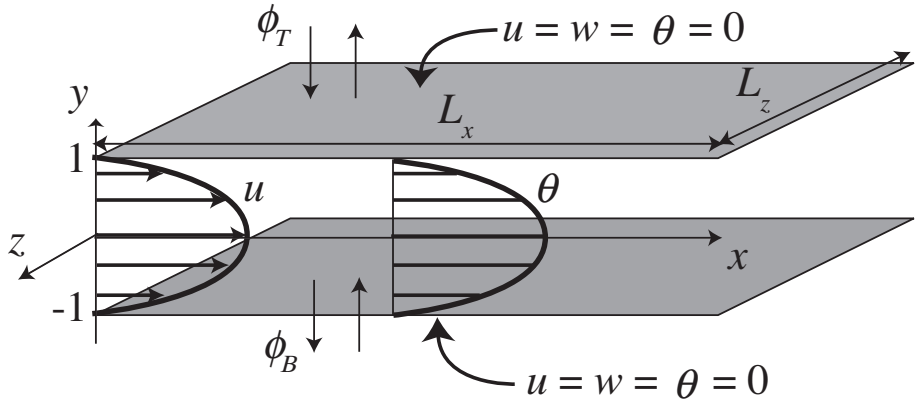

FIGURE 1. Computational domain and coordinate system

fully applied to turbulent drag reduction control (see, e.g., Lee et al. (1998); Fukagata & Kasagi (2004)). We will proceed as follows. We first describe the mathematical formulation in Sec. 2, and then derive a control law based on the suboptimal control theory in Sec. 3. In Sec. 4, we will show the global control performance of the present strategy, and then discuss the detailed mechanism of dissimilarity in Sec. 5. Based on the obtained knowledge, an open-loop strategy for dissimilar control is proposed and assessed in Sec. 6. Finally, we will summarize the conclusions in Sec. 7.

2. Mathematical Formulation and Numerical Conditions

2.1. *Governing equations and boundary conditions*

We consider a fully developed turbulent channel flow between two parallel plates as shown in Fig. 1. The streamwise, wall-normal and spanwise coordinates are denoted as x, y and z, respectively. Periodic boundary conditions are imposed in the x and z directions. The origin of y is located at the center of two walls, so that the locations of the bottom and top walls correspond to $y = -1$ and 1, respectively. The governing equations for the velocity field are given by the following Navier-Stokes and continuity equations:

$$\frac{\partial u_i}{\partial t} + \frac{\partial (u_j u_i)}{\partial x_j} = -\frac{\partial p}{\partial x_i} + \frac{1}{\mathrm{Re}} \frac{\partial u_i^2}{\partial x_j \partial x_j}, \tag{2.1}$$

$$\frac{\partial u_i}{\partial x_i} = 0. \tag{2.2}$$

Throughout this paper, all quantities are normalized by the bulk mean velocity U_b^* and the channel half width δ^* unless otherwise stated. The Reynolds number is defined as $\mathrm{Re} = U_b^* \delta^* / \nu^*$. Assuming the temperature as a passive scalar, the energy transport equation is given as:

$$\frac{\partial \theta}{\partial t} + \frac{\partial (u_j \theta)}{\partial x_j} = Q + \frac{1}{\mathrm{Pe}} \frac{\partial \theta^2}{\partial x_j \partial x_j}, \tag{2.3}$$

where Q represents a heat source, which is in general a function of space and time. The Peclet number is defined as a product of the Reynolds and Prandtl numbers, i.e., $\mathrm{Pe} = \mathrm{RePr}$.

In order to consider the special case in which the averaged momentum and heat transport equations are similar, we assume uniform heat generation in fluid, i.e., $Q = const.$, and

it is set to be equal to the mean pressure gradient as follows:

$$Q(x,y,z,t) = -\frac{\partial \overline{p}}{\partial x}. \tag{2.4}$$

Here, averaging is made over the homogeneous directions, i.e., x and z, and also time t. A typical example of the uniform heat generation is Joule heating of an aqueous solution of electrolytes. The resultant averaged momentum and heat transport equations are respectively derived as:

$$-\frac{\partial \overline{p}}{\partial x} = \frac{\partial}{\partial y}\left(\overline{u'v'} - \frac{1}{\mathrm{Re}}\frac{\partial \overline{u}}{\partial y}\right), \tag{2.5}$$

$$Q = -\frac{\partial \overline{p}}{\partial x} = \frac{\partial}{\partial y}\left(\overline{\theta'v'} - \frac{1}{\mathrm{Pe}}\frac{\partial \overline{\theta}}{\partial y}\right). \tag{2.6}$$

Throughout this study, the Prandtl number is kept constant as $\mathrm{Pr} = 1.0$ so that Pe in Eq. (2.6) reduces to Re. Consequently, Eqs. (2.5) and (2.6) have the same form. Hereafter, Pe is replaced by Re and θ is normalized by the cross-sectional average temperature Θ_m as defined later.

In the present study, we consider local wall blowing/suction with no net mass flux as a control input. As for the tangential velocity components and the temperature, we impose the no-slip and constant-temperature conditions at two walls. The resultant Dirichlet-type boundary conditions are given as:

$$u_i = \phi_B \delta_{i2}, \quad \theta = 0 \quad \text{at } y = -1 \tag{2.7}$$

$$u_i = \phi_T \delta_{i2}, \quad \theta = 0 \quad \text{at } y = 1, \tag{2.8}$$

where ϕ_B and ϕ_T are control inputs (given velocity) at the bottom and top walls, respectively. Note that the wall boundary conditions for the streamwise velocity component and the temperature remain similar even in the controlled flow, i.e., $u = \theta = 0$ at the walls.

2.2. *Numerical scheme and test conditions*

Equations (2.1)-(2.3) are solved by a pseudo-spectral method (essentially the same as that of Kasagi et al. (1992)), where Fourier expansion is employed in the x and z directions, while Chebyshev polynomials in the y direction. For time advancement, the second-order Adams-Bashforth and Crank-Nicolson methods are used for the convection and diffusion terms, respectively. All calculations are conducted under a constant bulk mean velocity with the Reynolds number $\mathrm{Re} = 2293$ unless otherwise stated. This corresponds to the friction Reynolds number of $\mathrm{Re}_\tau = u_\tau^* \delta^* / \nu^* = 150$ in uncontrolled flow. The computational domain size, the numbers of modes, and the corresponding grid spacings in the physical space are listed in Table 1. Note that the superscript of + denotes a quantity normalized by the viscous wall units of uncontrolled flow.

As will be shown below, the control input derived from the suboptimal control theory exhibits a traveling wave-like property, which is almost uniform in the spanwise direction and periodic in the streamwise direction. Therefore, we systematically change the streamwise length L_x of the computational domain (Cases 1-3) in order to investigate its effects on the optimized distribution of a control input and the control performance. In Case 2W, we double the spanwise domain size with the same grid spacing in order to ensure that the domain size does not affect the results. It is well known that the calculation of the scalar field at $\mathrm{Pr} = 1.0$ requires higher resolution than that for the velocity field due to the absence of the pressure gradient term in the energy transport equation. Hence, we double the number of modes in each direction in Case 1F to verify the present grid resolution. It is shown later that the effects of grid resolution on the control performance are commonly very small, since the present control generally modifies large-scale flow

TABLE 1. Computational domain widths, numbers of modes and grid spacings.

Re	L_x	L_z	$(N_x,\, N_y,\, N_z)$	$(\Delta x^+, \Delta y^+, \Delta z^+)$	$Case$
2293	2.5π	π	(64, 65, 64)	(18.4, 0.18−7.4, 7.4)	Case 1
2293	2.5π	π	(128, 129, 128)	(9.2, 0.045−3.7, 3.7)	Case 1F
2293	5.0π	π	(128, 65, 64)	(18.4, 0.18−7.4, 7.4)	Case 2
2293	5.0π	2π	(128, 65, 128)	(18.4, 0.18−7.4, 7.4)	Case 2W
2293	10.0π	π	(256, 65, 64)	(18.4, 0.18−7.4, 7.4)	Case 3
5055	2.5π	π	(128, 193, 128)	(18.4, 0.040−4.9, 7.4)	Case 4
8034	2.5π	π	(192, 257, 192)	(18.4, 0.034−5.5, 7.4)	Case 5

structures, which are resolved by a relatively coarse grid system. In all calculations, the time integration is repeated after the flow and thermal fields have reached a statistically steady state for more than $t = 400$, which corresponds to $t^+ \sim 4000$.

2.3. *Control performance indices*

The bulk mean velocity U_b^* is generally defined based on the total mass flow rate as:

$$U_b^* = \frac{1}{2\delta^*} \int_{-\delta^*}^{\delta^*} \overline{u^*} dy. \tag{2.9}$$

On the other hand, the bulk mean temperature Θ_b^*, which is also referred to as the mixing-cup temperature, is defined based on the total enthalpy flux as:

$$\Theta_b^* = \frac{\int_{-\delta^*}^{\delta^*} \overline{u^*\theta^*} dy}{\int_{-\delta^*}^{\delta^*} \overline{u^*} dy} = \frac{1}{2U_b^*\delta^*} \int_{-\delta^*}^{\delta^*} \overline{u^*\theta^*} dy, \tag{2.10}$$

of which rate of increase is equal to applied heat input. The above difference in the definitions of bulk mean quantities leads to quantitative difference between C_f and 2St even though the velocity and temperature profiles are similar. Since we are interested in the similarity solutions of u and θ, a different mean temperature is introduced to quantify the degree of dissimilarity. We employ the following cross-sectional mean temperature Θ_m:

$$\Theta_m^* = \frac{1}{2\delta^*} \int_{-\delta^*}^{\delta^*} \overline{\theta^*} dy. \tag{2.11}$$

The Stanton number St_m based on Θ_m can be defined by simply replacing Θ_b in Eq. (1.3) with Θ_m as:

$$\mathrm{St}_m = \frac{q_w^*}{\rho^* C_p^* U_b^* \Theta_m^*}. \tag{2.12}$$

By using St_m instead of St, $2\mathrm{St}_m/C_f$ is exactly equal to unity as long as the profiles of $\overline{u}$ and $\overline{\theta}$ are similar. In other words, the departure of $2\mathrm{St}_m/C_f$ from unity always indicates the dissimilarity between $\overline{u}$ and $\overline{\theta}$.

We remark on the quantitative relationship between the conventional St and St_m defined by Eqs. (1.3) and (2.12), respectively. In the present condition, Θ_m is smaller than Θ_b by about 6 % in uncontrolled flow so that St_m is estimated larger than the conventional St.

This trend is found to be slightly enhanced up to 10 % with increasing the magnitude of the control input. As a result, the above difference in the definitions of the bulk mean temperatures causes at most 4 % difference in the increase of the Stanton number above the value of uncontrolled flow. However, this fact hardly influences the present conclusions, since the present control commonly enhances St_m more drastically so that the effect of the definition of the bulk mean temperature always remains minor.

Recently, Fukagata et al. (2002) have derived a general mathematical relationship between the skin friction coefficient C_f and different dynamical contributions in wall-bounded flows. It is simplified to the following equation including two terms in a fully developed turbulent channel flows:

$$C_f = \frac{6}{\mathrm{Re}} + 3\int_{-1}^{1} y(\overline{u'v'})\, dy. \tag{2.13}$$

The first term on the RHS of Eq. (2.13) corresponds to the laminar drag, while the second the additional friction due to turbulence. The Reynolds shear stress $\overline{u'v'}$, which is weighted by y in the second term on the RHS of Eq. (2.13), implies that the Reynolds shear stress near the wall contributes more to the skin friction drag than that in the central region of the channel.

Similarly, we can also derive the following relationship for St_m:

$$2\mathrm{St}_m = \frac{6}{\mathrm{Re}} + 3\int_{-1}^{1} y(\overline{\theta'v'})\, dy, \tag{2.14}$$

which is exactly the same form as that of C_f in Eq. (2.13). Thus, it is obvious that dissimilarity between $\overline{u'v'}$ and $\overline{\theta'v'}$ is mandatory to achieve dissimilar control. According to Eq. (1.1), we introduce an analogy factor A as:

$$A = \frac{2\mathrm{St}_m}{C_f}. \tag{2.15}$$

Then, the main objective of this study is to demonstrate a possibility to increase A from unity by modifying turbulence.

The averaged momentum and energy equations (2.5) and (2.6) are also expressed with the eddy diffusivities for momentum E_v and heat E_c as:

$$-\frac{\partial \overline{p}}{\partial x} = -\frac{d}{dy}\left\{\left(E_v + \frac{1}{\mathrm{Re}}\right)\frac{d\overline{u}}{dy}\right\}, \tag{2.16}$$

$$-\frac{\partial \overline{p}}{\partial x} = -\frac{d}{dy}\left\{\left(E_c + \frac{1}{\mathrm{Re}}\right)\frac{d\overline{\theta}}{dy}\right\}, \tag{2.17}$$

where

$$E_v = \frac{-\overline{u'v'}}{\left(\dfrac{d\overline{u}}{dy}\right)}, \quad E_c = \frac{-\overline{\theta'v'}}{\left(\dfrac{d\overline{\theta}}{dy}\right)}. \tag{2.18}$$

Obviously, the similar solutions of $\overline{u}$ and $\overline{\theta}$ are obtained when $E_v = E_c$. According to the mixing length theory, both E_v and E_c are scaled by $u_t l_t$, where u_t and l_t are typical velocity- and length-scales of turbulence, respectively. We can also define the turbulent Prandtl number Pr_t analogous to the molecular Prandtl number as $\mathrm{Pr}_t = E_v/E_c$, which is a property of turbulence and represents the degree of local dissimilarity between turbulent momentum and heat transport mechanisms. Previous studies show that Pr_t is generally close to unity in a wide range of turbulent flows (see, e.g., Keys et al. (2005)). This fact supports the concept of the Reynolds analogy. On the other hand, in order to increase A from unity, E_c needs to be enhanced more than E_v, so that $\mathrm{Pr}_t^{-1} > 1.0$. Actually, this is achieved by the present control as will be shown later.

In active flow control, there always exists power consumption for the control itself. Therefore, from a practical viewpoint, the control power input P_c needs to be taken into account in evaluating the control performance. Applying a thermodynamic analysis to the flow system and the outer environment (see, Appendix A for more detailed discussions), the ideal power consumption of zero-net-mass-flux wall blowing/suction can be obtained as:

$$P_c^* = 2\overline{\left(p^{*\prime}v^{*\prime} + \frac{1}{2}\rho^* v^{*\prime 3}\right)}_w. \tag{2.19}$$

The subscript of w denotes a quantity at the wall, and the factor of two on the right-hand-side represents a sum of the work done on the two walls.

Hence, with P_p^* being the pumping power, the total net power consumption is obtained as:

$$P_{total}^* = P_p^* + P_c^* = 2\left(-\frac{d\overline{p^*}}{dx^*}\right)U_b^*\delta^* + 2\overline{\left(p^{*\prime}v^{*\prime} + \frac{1}{2}\rho^* v^{*\prime 3}\right)}_w. \tag{2.20}$$

Considering the fact that the pumping power is proportional to the wall friction under a constant mass flow rate, we define the equivalent wall friction $(\tau_w)_{net}$ based on the above power consumption in controlled flow as:

$$(\tau_w^*)_{net} = \frac{P_{total}^*}{2U_b^*} = -\left(\frac{d\overline{p^*}}{dx^*}\right)\delta^* + \frac{1}{U_b^*}\overline{\left(p^{*\prime}v^{*\prime} + \frac{1}{2}\rho^* v^{*\prime 3}\right)}_w. \tag{2.21}$$

By using $(\tau_w^*)_{net}$, we define the corresponding friction coefficients as $C_{f\,net} = (\tau_w^*)_{net}/(\rho^* U_b^{*2}/2)$. Similarly, the analogy factors are also defined as $A_{net} = 2\mathrm{St}_m/C_{f_{net}}$. Physically, A_{net} represents heat transfer per a unit total power consumption. In the following, the control performance is evaluated with the above two factors, i.e., A and A_{net}.

3. Application of Suboptimal Control Theory to Dissimilar Heat Transfer Enhancement

3.1. *Derivation of differential state*

Following Lee et al. (1998), we discretize the Navier-Stokes and energy equations so that the diffusion and pressure gradient terms are treated implicitly, while the advection terms explicitly. This results in the following equations representing the short-time dynamics of the system:

$$u_i^{n+1} + \frac{\Delta t}{2}\frac{\partial p^{n+1}}{\partial x} - \frac{\Delta t}{2\mathrm{Re}}\frac{\partial^2 u_i^{n+1}}{\partial x_j \partial x_j} = R^n, \tag{3.1}$$

$$\frac{\partial u_i^{n+1}}{\partial x_i} = 0, \tag{3.2}$$

$$\theta^{n+1} - \frac{\Delta t}{2\mathrm{Re}}\frac{\partial^2 \theta^{n+1}}{\partial x_j \partial x_j} = Q^n. \tag{3.3}$$

We introduce a Fréchet differential in order to define the differential states of the velocity, pressure and temperature (q_i, σ, η) as:

$$q_i = \frac{\mathscr{D}u_i(\phi)}{\mathscr{D}\phi}\tilde{\phi}, \tag{3.4}$$

$$\sigma = \frac{\mathscr{D}p(\phi)}{\mathscr{D}\phi}\tilde{\phi}, \tag{3.5}$$

$$\eta = \frac{\mathscr{D}\theta(\phi)}{\mathscr{D}\phi}\tilde{\phi}. \tag{3.6}$$

Here, $\tilde{\phi}$ is arbitrary perturbation field to ϕ. Applying the Fréchet differential to the above equations, the governing equations for differential states (q_i, σ, η) are obtained as:

$$q_i + \frac{\Delta t}{2}\frac{\partial \sigma}{\partial x_i} - \frac{\Delta t}{2\mathrm{Re}}\frac{\partial^2 q_i}{\partial x_j \partial x_j} = 0, \tag{3.7}$$

$$\frac{\partial q_i}{\partial x_i} = 0, \tag{3.8}$$

$$\eta - \frac{\Delta t}{2\mathrm{Re}}\frac{\partial^2 \eta}{\partial x_j \partial x_j} = 0. \tag{3.9}$$

Here, we consider wall blowing/suction as a control input so that the wall boundary conditions for differential states are

$$q_i = \tilde{\phi}_B \delta_{i2}, \;\; \theta = 0 \text{ at } y = -1, \tag{3.10}$$

$$q_i = \tilde{\phi}_T \delta_{i2}, \;\; \theta = 0 \text{ at } y = 1, \tag{3.11}$$

where $\tilde{\phi}_B$ and $\tilde{\phi}_T$ are perturbations to the control inputs at the bottom and top walls, respectively. Solving Eqs. (3.7)-(3.9) under the boundary conditions (3.10) and (3.11), we obtain the following approximated solutions:

$$\begin{aligned}\widehat{q_1}(y) \;\; = \frac{ik_1}{k\cdot\sinh(2k)}\Bigg[& \;\; \widehat{\tilde{\phi}}_T \cosh\{k(y+1)\} - \widehat{\tilde{\phi}}_B \cosh\{k(y-1)\} \\ & -\left\{\widehat{\tilde{\phi}}_T \cosh(2k) - \widehat{\tilde{\phi}}_B\right\}\exp\left\{-\sqrt{\frac{2\mathrm{Re}}{\Delta t}}(1-y)\right\} \\ & -\left\{\widehat{\tilde{\phi}}_T - \widehat{\tilde{\phi}}_B \cosh(2k)\right\}\exp\left\{-\sqrt{\frac{2\mathrm{Re}}{\Delta t}}(y+1)\right\}\Bigg],\end{aligned} \tag{3.12}$$

$$\begin{aligned}\widehat{q_3}(y) \;\; = \frac{ik_3}{k\cdot\sinh(2k)}\Bigg[& \;\; \widehat{\tilde{\phi}}_T \cosh\{k(y+1)\} - \widehat{\tilde{\phi}}_B \cosh\{k(y-1)\} \\ & -\left\{\widehat{\tilde{\phi}}_T \cosh(2k) - \widehat{\tilde{\phi}}_B\right\}\exp\left\{-\sqrt{\frac{2\mathrm{Re}}{\Delta t}}(1-y)\right\} \\ & -\left\{\widehat{\tilde{\phi}}_T - \widehat{\tilde{\phi}}_B \cosh(2k)\right\}\exp\left\{-\sqrt{\frac{2\mathrm{Re}}{\Delta t}}(y+1)\right\}\Bigg],\end{aligned} \tag{3.13}$$

$$\widehat{q_2}(y) \;\; = \frac{1}{\sinh(2k)}\Bigg[\;\; \widehat{\tilde{\phi}}_T \sinh\{k(y+1)\} - \widehat{\tilde{\phi}}_B \sinh\{k(y-1)\}\Bigg], \tag{3.14}$$

$$\hat{\sigma}(y) = \frac{-2}{\Delta t\cdot k\cdot\sinh(2k)}\Bigg[\widehat{\tilde{\phi}}_T \cosh\{k(y+1)\} - \widehat{\tilde{\phi}}_B \cosh\{k(y-1)\}\Bigg], \tag{3.15}$$

$$\hat{\eta}(y) \;\; = 0. \tag{3.16}$$

Here, a variable with a hat represents a Fourier coefficient and $k = \sqrt{k_1^2 + k_3^2}$, where k_1 and k_3 are wavenumbers in the x and z directions, respectively. The above solutions are obtained with an assumption of $2\mathrm{Re}/\Delta t \gg k^2$. The obtained differential states (3.12)−(3.15) of the velocity fields are slightly different from those derived by Lee et al. (1998), since they assume that the length-scale of a control input is much smaller than the channel half depth, i.e., $k \gg 1$, so that the effect of the opposing wall can be neglected. In the present study, however, the resultant control input has a large-scale coherent structure as will be shown later. Hence, the joint effect of the two walls is taken into account in deriving Eqs. (3.12)−(3.16). Obviously, the present solutions converge to those obtained by Lee et al. (1998) when $k \gg 1$.

Some remark should be given to the difference between the solutions of the streamwise velocity component and the temperature given by Eqs. (3.12) and (3.16). When wall blowing/suction is applied, the pressure field instantaneously reacts to it and redistributes the kinetic energy of the wall-normal velocity fluctuation to the tangential components. This

is caused by the continuity constraint on the velocity field. In the case of the scalar field, however, there exists no pressure-gradient term in Eq. (3.9), and therefore η vanishes (see, Eq. (3.16)). This fact shows an essential difference between the responses of the velocity and scalar fields to the control input and suggests a possibility of dissimilar control. Equation (3.16) seems to indicate that the wall blowing/suction of low-temperature fluid has no impact on the temperature field. Actually, we can obtain a non-trivial response of the temperature field by implicitly treating the advection terms in Eq. (3.3). It should be noted, however, that the advection terms have similar forms in the momentum and energy equations so that they do not cause dissimilarity. Hence, the present formulation is sufficient to count the inherent difference between the divergence-free vector and the conservative scalar.

3.2. *Defining cost function*

We define the cost function J as follows:

$$J = \frac{1}{S\Delta t}\int_S\int_t^{t+\Delta t}\frac{1}{2}(\phi_T^2+\phi_B^2)dtdS + \frac{\beta}{V\Delta t}\int_V\int_t^{t+\Delta t} yu_1'u_2'\,dtdV - \frac{\gamma}{V\Delta t}\int_V\int_t^{t+\Delta t} y\theta'u_2'\,dtdV, \tag{3.17}$$

where the temporal integration is made over a short duration of computational time step Δt. The spatial integration is also made over the wall surface (S) for the first term, whilst over the whole flow domain (V) for the second and third terms. Our goal is to deduce the optimal spatio-temporal distribution of control input ϕ to minimize J.

The first term on the RHS of Eq. (3.17) represents the cost of actuation. In accordance with Eqs. (2.13) and (2.14), we add the weighted Reynolds stress and weighted turbulent heat flux, which appear as the second and third terms, in order to evaluate friction drag and heat transfer, respectively. The coefficients of β and γ correspond to the relative costs (or merits) of friction drag and heat transfer to the control input, respectively. We give a negative sign to the third term so as to seek the least control input that maximizes the heat transfer while reducing the friction drag. It should be noted that it is possible to include A explicitly in the cost function. In this case, it can be shown that the resultant Fréchet differential of J reduces to the same form as that obtained by the present cost function (3.17) (see, Appendix B). Therefore, the present cost function (3.17) is consider as a general form for dissimilar control.

Applying the Fréchet differential to Eq. (3.17), we obtain

$$\begin{aligned}\frac{\mathscr{D}J}{\mathscr{D}\phi}\tilde{\phi} = {}& \frac{1}{S\Delta t}\int_S\int_t^{t+\Delta t}\phi_B\tilde{\phi}_B+\phi_T\tilde{\phi}_T dtdS \\ & + \frac{\beta}{V\Delta t}\int_V\int_t^{t+\Delta t} y(q_1u_2'+u_1'q_2)dtdV \\ & - \frac{\gamma}{V\Delta t}\int_V\int_t^{t+\Delta t} y(\eta u_2'+\theta' q_2)dtdV.\end{aligned} \tag{3.18}$$

The above equation can be converted into Fourier components as:

$$\begin{aligned}\widehat{\frac{\mathscr{D}J}{\mathscr{D}\phi}}\hat{\tilde{\phi}}^* = {}& \hat{\phi}_B\hat{\tilde{\phi}}_B^* + \hat{\phi}_T\hat{\tilde{\phi}}_T^* \\ & + \beta\int_{-1}^{1} y(\hat{u_2'}\hat{q_1}^* + \hat{u_1'}\hat{q_2}^*)dy \\ & - \gamma\int_{-1}^{1} y(\hat{u_2'}\hat{\eta}^* + \hat{\theta'}\hat{q_2}^*)dy.\end{aligned} \tag{3.19}$$

Substituting Eqs.(3.12)−(3.16) to Eq. (3.19), we obtain

$$\begin{aligned}
&\widehat{\frac{\mathscr{D}J}{\mathscr{D}\phi}}\hat{\tilde{\phi}}^* = \\
&\hat{\tilde{\phi}}_B^*\Bigg[\hat{\phi}_B + \beta\int_{-1}^{1} y\Bigg\{\frac{ik_1\cosh\{k(y-1)\}}{k\cdot\sinh(2k)}\hat{u}_2(y) - \frac{\sinh\{k(y-1)\}}{\sinh(2k)}\hat{u}_1(y)\Bigg\}dy \\
&\qquad + \gamma\int_{-1}^{1} y\Bigg\{\frac{\sinh\{k(y-1)\}}{\sinh(2k)}\hat{\theta}(y)\Bigg\}dy\Bigg] \\
&+\hat{\tilde{\phi}}_T^*\Bigg[\hat{\phi}_T - \beta\int_{-1}^{1} y\Bigg\{\frac{ik_1\cosh\{k(y+1)\}}{k\cdot\sinh(2k)}\hat{u}_2(y) - \frac{\sinh\{k(y+1)\}}{\sinh(2k)}\hat{u}_1(y)\Bigg\}dy \\
&\qquad - \gamma\int_{-1}^{1} y\Bigg\{\frac{\sinh\{k(y+1)\}}{\sinh(2k)}\hat{\theta}(y)\Bigg\}dy\Bigg] \\
&+O\left(\sqrt{\frac{\Delta t}{\mathrm{Re}}}\right).
\end{aligned} \tag{3.20}$$

Here, we neglect the contributions from the third and forth terms in the square bracket in Eq. (3.12) to the integrals in Eq. (3.19), since they have significant values only in the near-wall region whose thickness is very thin and the order of $\sqrt{\Delta t/\mathrm{Re}}$.

Minimizing the Fréchet differential of the cost function requires $\mathscr{D}J/\mathscr{D}\phi = 0$, and the control inputs ϕ_B and ϕ_T are eventually deduced as follows:

$$\begin{aligned}
\hat{\phi}_B = \quad & \beta\int_{-1}^{1} y\Bigg\{\frac{\sinh\{k(y-1)\}}{\sinh(2k)}\hat{u}_1(y) - \frac{ik_1\cosh\{k(y-1)\}}{k\cdot\sinh(2k)}\hat{u}_2(y)\Bigg\}dy \\
& - \gamma\int_{-1}^{1} y\Bigg\{\frac{\sinh\{k(y-1)\}}{\sinh(2k)}\hat{\theta}(y)\Bigg\}dy,
\end{aligned} \tag{3.21}$$

$$\begin{aligned}
\hat{\phi}_T = \quad & \beta\int_{-1}^{1} y\Bigg\{-\frac{\sinh\{k(y+1)\}}{\sinh(2k)}\hat{u}_1(y) + \frac{ik_1\cosh\{k(y+1)\}}{k\cdot\sinh(2k)}\hat{u}_2(y)\Bigg\}dy \\
& + \gamma\int_{-1}^{1} y\Bigg\{\frac{\sinh\{k(y+1)\}}{\sinh(2k)}\hat{\theta}(y)\Bigg\}dy.
\end{aligned} \tag{3.22}$$

It should be mentioned that the present control law requires the complete information over the whole flow domain at each time instant, based on which the wall blowing/suction is applied. This is in contrast to the previous control laws derived by Lee et al. (1998) and Fukagata & Kasagi (2004), in which the cost function is defined by using the surface integral of the information only on the wall. Although collecting the state information over the whole domain is not feasible in reality, it is justified by our main objectives to demonstrate a dissimilar control and to obtain general knowledge for dissimilar control by exploring the resultant controlled velocity and temperature fields.

4. Control Results

4.1. *Validation of Control Strategy*

In order to present an overall picture how the present control strategy works, we focus on the global control performance indices in this section. First, we show typical results with different combinations of the relative costs of drag reduction and heat transfer, i.e., β and γ. According to Eq. (3.17), we refer to the cases with $(\beta > 0, \gamma > 0)$ as dissimilar control, whereas those with $(\beta > 0, \gamma = 0)$ and $(\beta = 0, \gamma > 0)$ as drag reduction and heat transfer enhancement controls, respectively. In the present study, the magnitudes of the

control inputs relative to the bulk mean velocity U_b at the two walls are kept constant by rescaling Eqs. (3.21) and (3.22) at every time step, so that only the ratio of β and γ is of concern. This is not the case in the drag reduction control, since the magnitude of the control input needs to be adjusted to an instantaneous turbulence state in order to avoid additional flow instabilities, which eventually cause drag increase. Hence, in the drag reduction control, β is specified at the onset of the control so that the magnitude of the control input coincides with a prescribed value, and the rescaling of the control input is not implemented during calculation.

In Fig. 2, the friction coefficient C_f and the Stanton number St_m are shown as a function of time from the onset of the control. The mangnitude (root-mean-square value) of the control input at each wall is set to be 2 % of the bulk mean velocity, i.e., $\phi_{rms} = 0.02$. In the dissimilar and heat transfer controls, both C_f and St_m are increased, although they are both decreased in the drag reduction control. The highest St_m is achieved in the heat transfer control.

For comparison, we also plot the results in the opposition control for drag reduction proposed by Choi et al. (1994), where the local blowing/suction is applied in proportion to the wall-normal velocity fluctuation at a detection plane located above the wall. In the present study, the detection plane is located at $y^+ = 10$ and the proportional constant is set to be unity. Compared to the opposition control, the present drag reduction control does not result in significant improvement in the drag reduction rate, although the information in the whole flow domain is supplied. Since the weighted Reynolds shear stress has a peak around $y^+ = 20$ at the present Reynolds number of $\mathrm{Re}_\tau = 150$ (see, Fukagata & Kasagi (2004), Kasagi et al. (2009)), the present control input has the largest negative correlation (as large as -0.5) with the wall normal velocity fluctuation around this location. As reported in the study of opposition control (Choi et al. (1994), Fukagata & Kasagi (2004)), however, when the distance of the detection plane from the wall becomes larger than $y^+ = 15$, the control performance starts to decline due to the rapid recovery of the weighted Reynolds shear stress near the wall. Lim & Kim (2004) also show that the opposition control using a detection plane too far away from the wall enhances the transient growth rate of the optimal disturbance. Such energy amplification in finite time period is obviously not taken into account in the framework of the suboptimal control theory. This would be a primary reason for the relatively low drag reduction rate in the present control.

In Fig. 3, the time traces of analogy factor $A = 2\mathrm{St}_m/C_f$ for different values of β and γ are shown. The highest dissimilarity is achieved in the dissimilar control. It should also be noted that A becomes larger than unity in the heat transfer control as well, but it remains around unity in the drag reduction control and the opposition control. The general trend observed in Figs. 2 and 3 is consistent with the rationale of the cost function, and therefore suggests the validity of the present control strategy. In the following, we focus on the dissimilar control, i.e., the case with $(\beta, \gamma) = (1, 1)$.

4.2. *Effects of Control Input Amplitude in Dissimilar Control*

4.2.1. *Control performance*

The time traces of C_f and St_m for the dissimilar control with different control input amplitudes are shown in Fig. 4. The relative magnitude to the bulk velocity is changed as $\phi_{\mathrm{rms}} = 0.01, 0.02, 0.05$ and 0.1. With increasing ϕ_{rms}, both C_f and St_m first increase and then abruptly decrease at $\phi_{\mathrm{rms}} = 0.1$. In Fig. 5, the analogy factor A at each control amplitude ϕ_{rms} is shown. In the uncontrolled flow, similarity between the velocity and temperature fields holds almost completely, i.e., $A \approx 1$. By applying the control, A is enhanced up to about 1.5 with increasing ϕ_{rms}, and then saturating at $\phi_{\mathrm{rms}} > 0.05$.

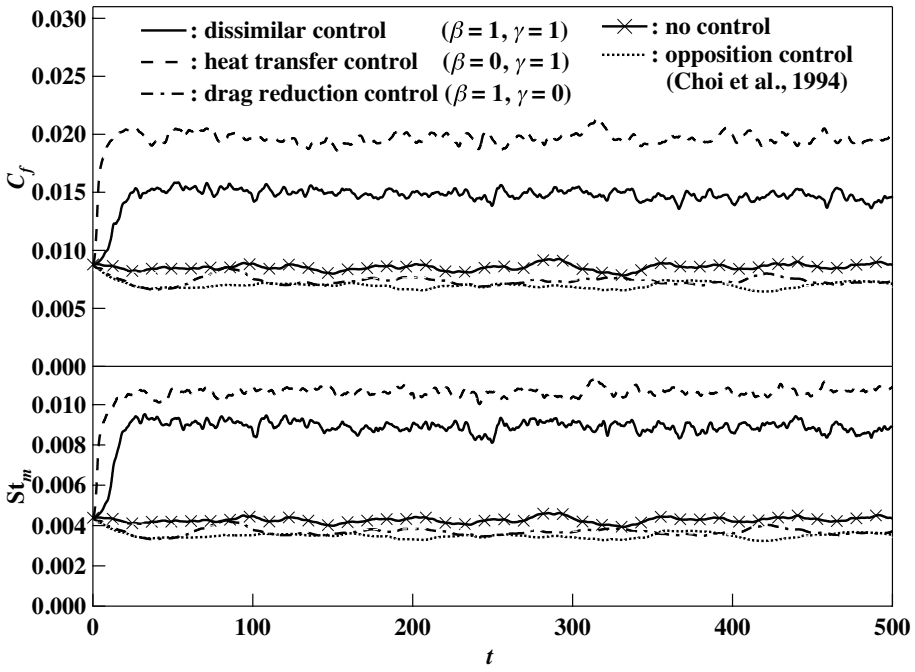

FIGURE 2. Time traces of friction coefficient C_f and Stanton number St_m for different values of β and γ at $\phi_{rms} = 0.02$.

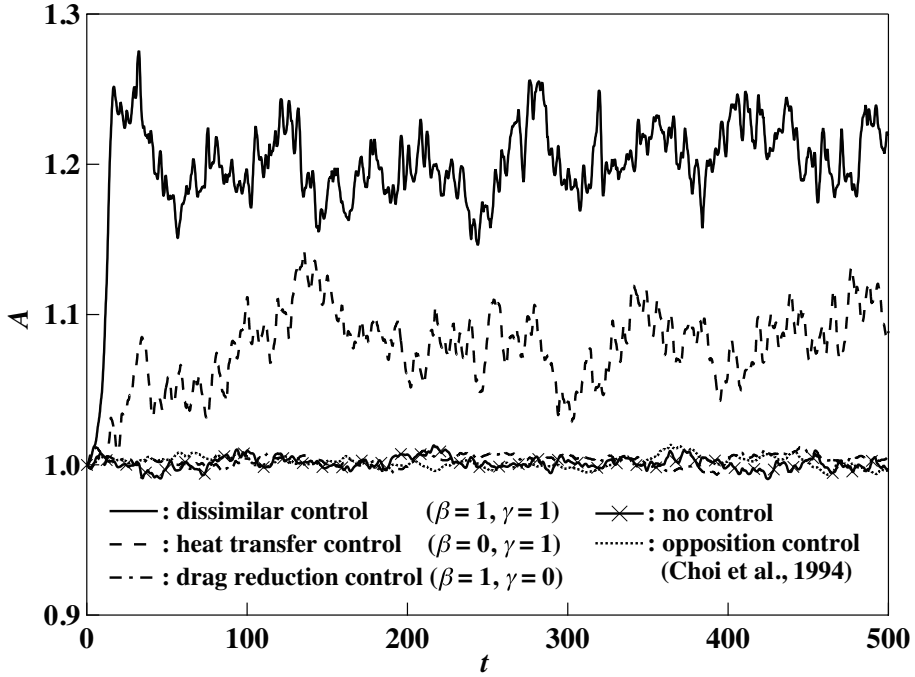

FIGURE 3. Time traces of analogy factor $A = 2\mathrm{St}_m/C_f$ for different values of β and γ at $\phi_{rms} = 0.02$.

The control results with different ϕ_{rms} are summarized in Table 2. When $\phi_{rms} \leq 0.05$, A_{net} is slightly larger than A. This indicates $(\tau_w)_{net} < \tau_w$, and therefore positive net energy recovery from the flow field, i.e., $P_c < 0$ (see, Eq. (2.21) and also Appendix A for more general discussions). In contrast, at the large amplitude of $\phi_{rms} = 0.1$, A_{net} becomes smaller than A. Simulations were also repeated with the finer grid system (Case

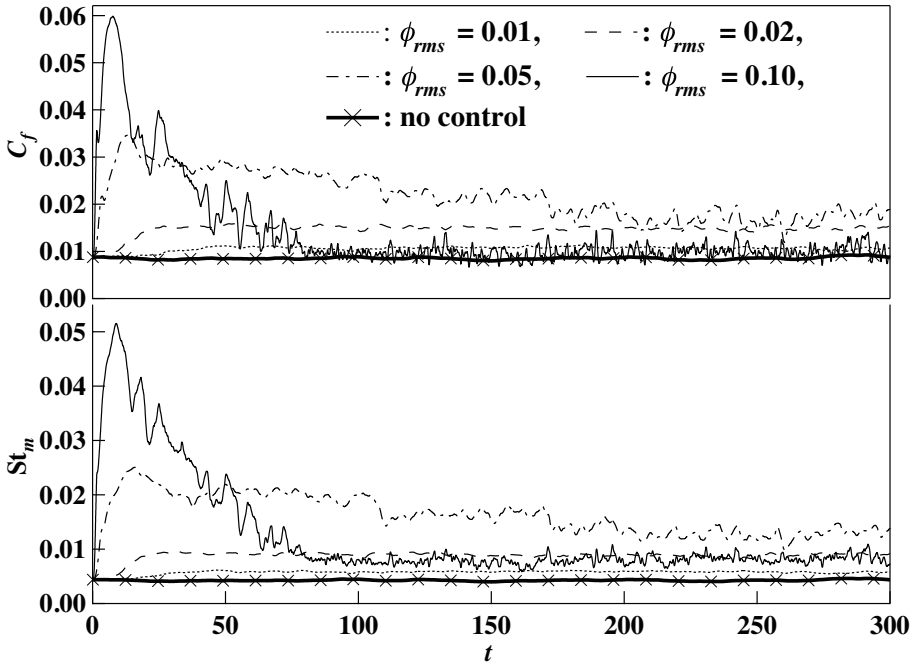

FIGURE 4. Time traces of C_f and St_m in the dissimilar control for different ϕ_{rms}.

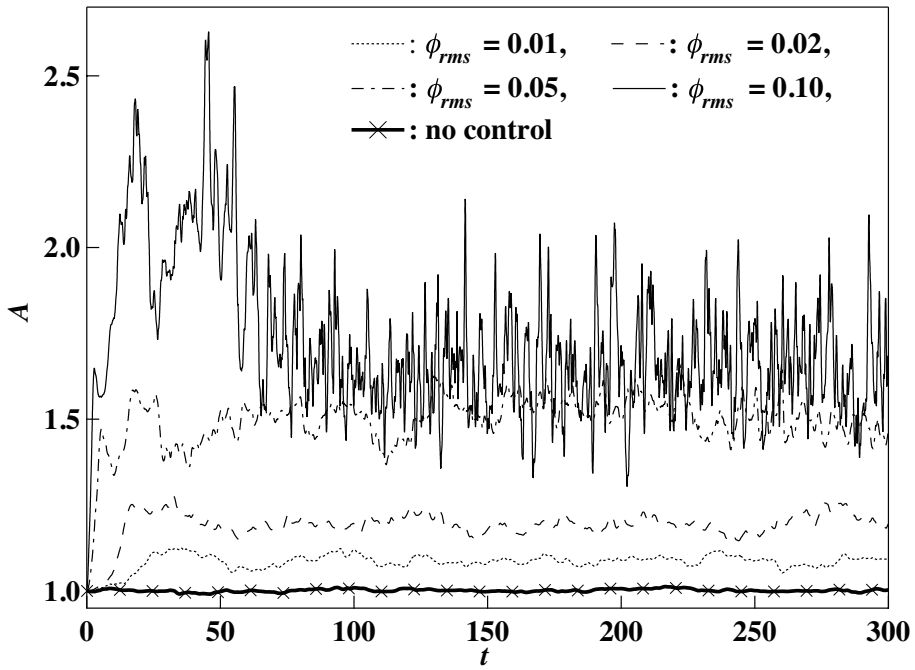

FIGURE 5. Time traces of A in the dissimilar control for different ϕ_{rms}.

1F in Table 1) for large amplitudes, i.e., $\phi_{\mathrm{rms}} = 0.05$ and 0.1. It is confirmed that the effects of the grid resolution are negligibly small in both cases (see, Table 2). Hereafter, we focus on the cases with small amplitudes, i.e., $\phi_{\mathrm{rms}} \leq 0.05$, because they achieve significant heat transfer enhancement with large A and A_{net} as listed in Table 2.

TABLE 2. Control results with different amplitudes of the control input

ϕ_{rms}	$C_f \cdot 10^2$	$\mathrm{St}_m \cdot 10^2$	A	A_{net}	U_p	$\langle\phi\rangle_{\mathrm{rms}}/\phi_{\mathrm{rms}}$	grid
0 (no control)	0.858	0.430	1.00	–	–	–	Case 1
0.01	1.06	0.577	1.09	1.12	0.353	0.779	Case 1
0.02	1.46	0.882	1.21	1.31	0.380	0.804	Case 1
0.05	1.74	1.31	1.51	1.61	0.277	0.657	Case 1
0.05	1.78	1.32	1.48	1.58	0.295	0.652	Case 1F
0.10	0.963	0.782	1.64	1.36	–	–	Case 1
0.10	0.968	0.790	1.64	1.36	–	–	Case 1F

4.2.2. *Features of the control input*

In Fig. 6, three successive snap-shots of the instantaneous control input at both walls for $\phi_{rms} = 0.05$ are shown. The time interval between them is $\Delta t = 7.3$, and the left and right figures show the control inputs on the bottom and top walls, respectively. Note that the wall-normal velocity component ϕ at the wall is plotted with solid and dotted lines, which represent blowing and suction at the two walls, respectively. For convenience, strong blowing regions with $\phi > 0.06$ at the bottom wall and $\phi < -0.06$ at the top wall are highlighted by thick solid lines. It is found that strong blowing localized in a narrow spanwise band exists being sandwiched by relatively weak suction regions in the upstream and downstream.

This coherent pattern of the control input is found to travel in the downstream direction at an almost constant speed. In addition, the control input seems to be introduced in a varicose-mode, namely, when ϕ is positive (wall blowing) on the bottom wall, negative ϕ (also wall blowing) is found on the opposite top wall. It should be noted that such traveling wave-like control input is observed only for small magnitudes of the control input, i.e., when $\phi_{rms} \leq 0.05$, while blowing and suction appear randomly over the wall at $\phi_{rms} = 0.1$. This would be a reason for the drastic decrease of C_f and St_m at $\phi_{rms} = 0.1$ (see, Table 2).

In order to examine a coherent component in the traveling wave-like control input, we employ a conditional averaging technique. First, the instantaneous control input at the bottom wall is averaged in the spanwise direction and the location x_p where the spanwise-averaged wall blowing becomes maximum is identified. Then, the control input at each wall is averaged with respect to x_p over a sufficiently long period after the velocity and thermal fields reach the fully developed state. As a result, the instantaneous control inputs ϕ at the two walls can be described as:

$$\phi(x, z, t) = \langle\phi\rangle(x - x_p(t)) + \phi''(x - x_p(t), z, t), \tag{4.1}$$

where the angle bracket represents the conditional averaging, while the double prime the deviation from the conditionally-averaged value. Note that x_p is a function of time and determined based on the control input at the bottom wall only, so that $\langle\phi\rangle$ at the top wall has a significant value only when the control inputs at the two walls are highly correlated.

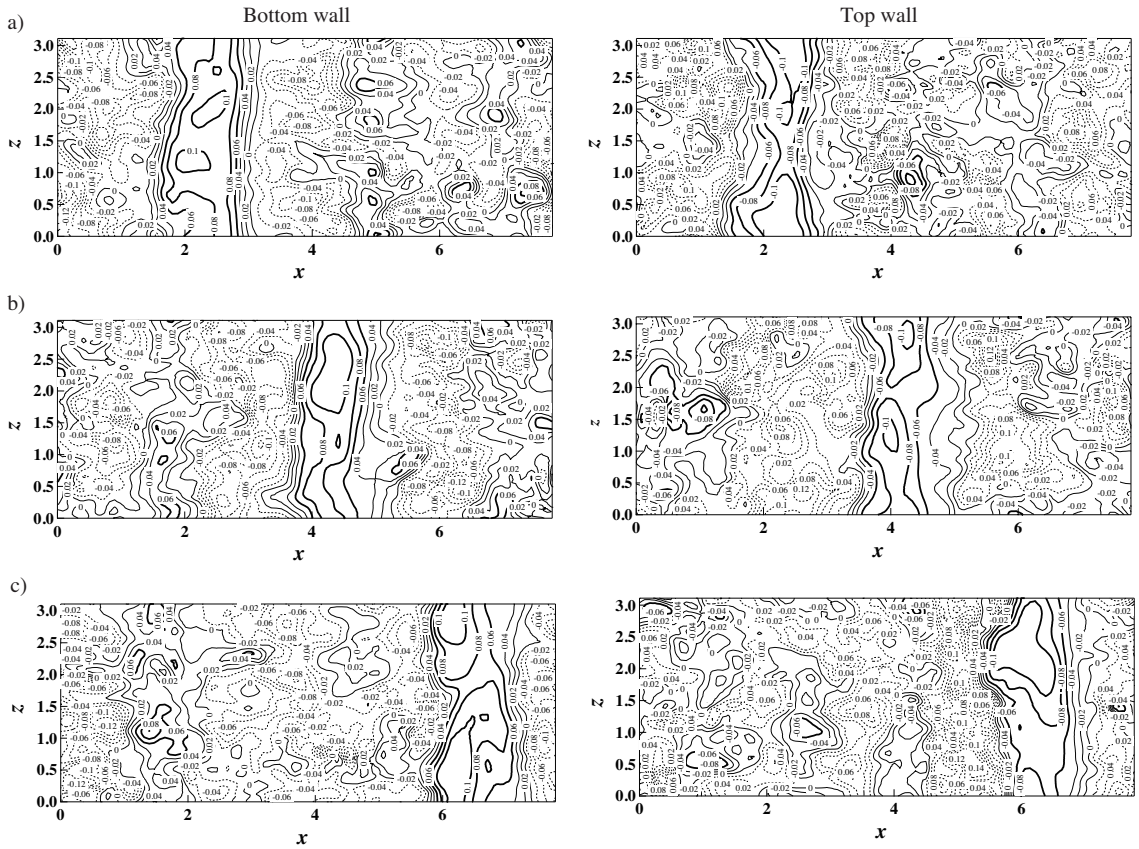

FIGURE 6. Three successive snapshots of instantaneous control input ϕ at bottom and top walls with a time interval of $\Delta t = 7.3$. Blowing regions are depicted by solid lines, while suction regions by dotted lines. Strong blowing regions ($\phi > 0.06$ and $\phi < -0.06$ at bottom and top walls, respectively) are represented by thick lines.

The conditionally-averaged control inputs $\langle\phi_B\rangle$ and $\langle\phi_T\rangle$ at the bottom and top walls are shown in Fig. 7. Surprisingly, $\langle\phi_B\rangle$ and $\langle\phi_T\rangle$ are almost symmetric, indicating that the control is in a varicose-mode. With increasing $\phi_{\rm rms}$, the region with strong blowing becomes narrower and more pronounced, whereas weaker suction regions extends upstream of the blowing region. The ratio of the root-mean-square value of the coherent component and that of the instantaneous control input is listed in Table 2. The coherent component commonly accounts for large portion of the instantaneous control input, namely, about $65 - 80$ % of the root-mean-square value.

The trajectories of x_p at different amplitudes of the control input are shown in Fig. 8. They are almost straight lines, suggesting that these waves travel at a constant speed. The phase speed, i.e., $U_p = \overline{dx_p/dt}$, is 30-40 % of the bulk mean velocity as summarized in Table 2. Taking a closer look, it is also found that the phase speed shows non-monotonous behavior with ϕ_{rms}. Namely, U_p becomes maximum when $\phi_{rms} = 0.02$. Note that the results with the finer grid system (Case 1F in Table 1) are also plotted in Figs. 7 and 8, which show that the grid dependency is minor.

The present control input derived from the suboptimal control theory has a similar distribution that used in Kong et al. (2001), where blowing from a spanwise slot is found to cause stronger dissimilarity than suction, although the slot location is fixed in their study. It has also been reported that streamwise-periodic wall blowing and suction in the form of an upstream traveling wave leads to drag reduction in turbulent channel flow at a low Reynolds number (Min et al. 2006). In the present control, the drag is

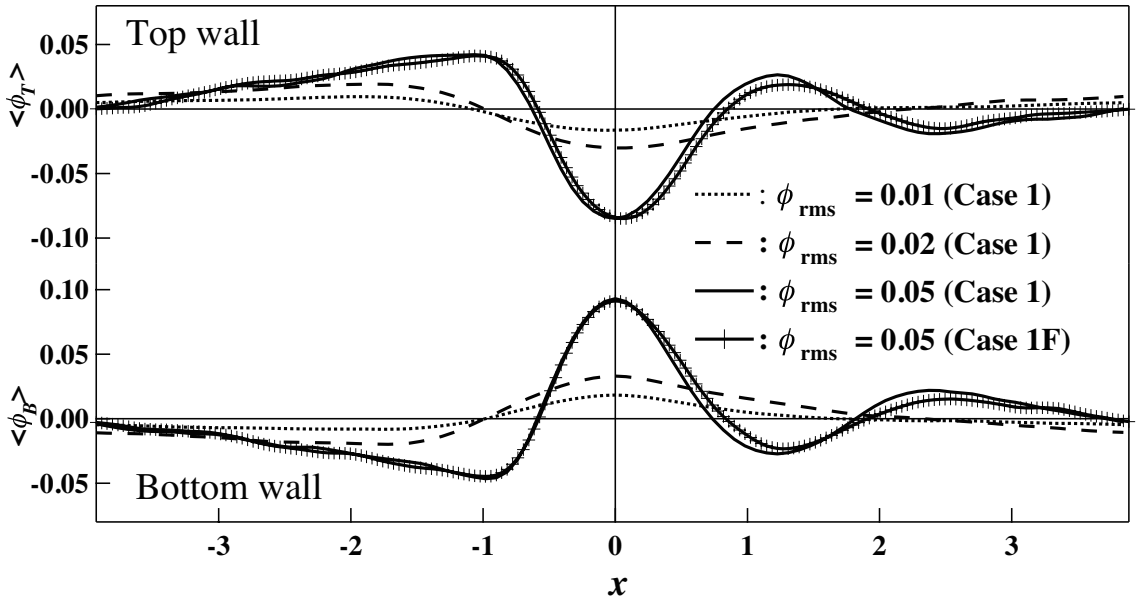

FIGURE 7. Conditionally-averaged control inputs $\langle\phi\rangle$ at the top and bottom walls.

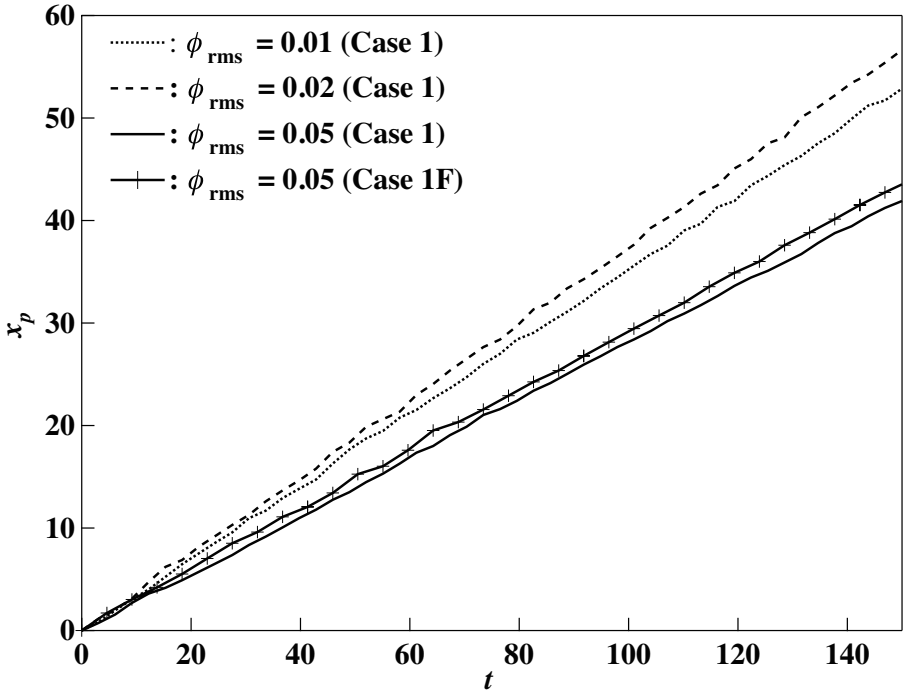

FIGURE 8. Time traces of the peak location x_p of the spanwise-averaged wall blowing.

increased with a downstream traveling wave-like control, but the heat transfer is more enhanced, and therefore the dissimilar control is achieved (see, Figs. 4 and 5). We also note that a similar traveling wave-like control input is obtained when the control is applied on a single wall only (see, Appendix C).

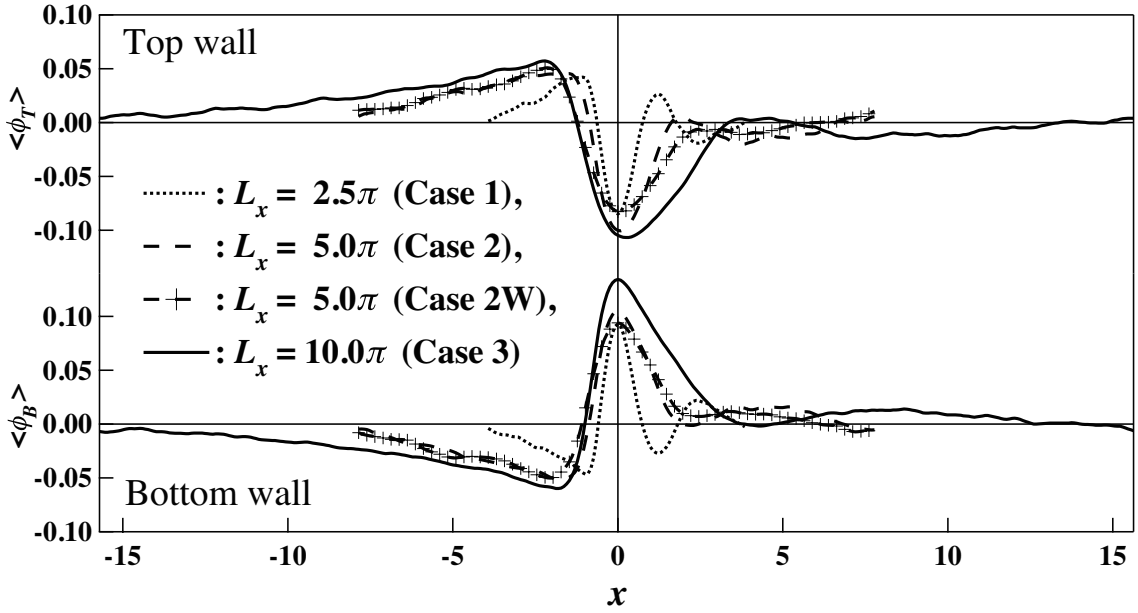

FIGURE 9. Conditionally-averaged control inputs $\langle\phi\rangle$ at the top and bottom walls for different streamwise domain lengths L_x at $\phi_{\rm rms} = 0.05$.

4.3. *Effects of Domain Size*

In order to investigate the effects of the domain size on the traveling wave-like control input and the resultant control performance, we systematically change the streamwise domain length as $L_x = 2.5\pi, 5.0\pi$ and 10.0π with keeping the amplitude of the control input as $\phi_{\rm rms} = 0.05$. The conditionally-averaged control inputs $\langle\phi\rangle$ at different L_x are shown in Fig. 9. In all cases, we obtain a single spanwise band with localized blowing. In the upstream of the wall blowing, there is a relatively wide area of weak wall suction. This suction region extends further upstream with increasing L_x. In contrast, in the downstream of the maximum blowing location, the control input decreases rather gradually to zero and no significant suction is observed.

The features of the traveling wave and the control performances are summarized in Table 3. In all cases, the conditionally-averaged control input $\langle\phi\rangle$ accounts for around 70 % of the root-mean-square control input ϕ, and travels in the downstream direction at a constant speed of 20-30 % of the bulk mean velocity, whereas the phase velocity is slightly decreased in the long computational domain of $L_x = 10\pi$. Note that the results with the spanwise doubled domain, i.e., case 2W, are also presented in Fig. 9 and Table 3. It is confirmed that L_z does not significantly affect the present results.

As for the control performance, with increasing L_x, both C_f and St_m are enhanced, whereas they almost saturate for $L_x > 5.0\pi$ (see, Table 3). The analogy factor A is kept as large as 1.5 and almost independent of L_x. The monotonic increase in A_{net} with L_x implies more energy recovery from the flow field. In summary, the streamwise periodic length L_x affects neither the main features of the traveling wave-like control input nor the control performances significantly. This would be beneficial in practical applications, since the wall blowing can be applied at lower frequency in the streamwise direction. With increasing L_x, however, the local blowing needs to be more intensified when ϕ_{rms} is kept constant as shown in Fig. 9.

TABLE 3. Control results for different streamwise domain lengths L_x at $\phi_{\rm rms} = 0.05$.

L_x	$C_f \cdot 10^2$	$\mathrm{St}_m \cdot 10^2$	A	A_{net}	U_p	$\langle\phi\rangle_{\rm rms}/\phi_{\rm rms}$	grid
2.5π	1.74	1.31	1.51	1.61	0.277	0.657	Case 1
5.0π	2.40	1.82	1.51	1.75	0.286	0.724	Case 2
5.0π	2.48	1.84	1.48	1.71	0.268	0.693	Case 2W
10.0π	2.48	1.93	1.55	1.85	0.215	0.740	Case 3

TABLE 4. Reynolds number effects on control results at $\phi_{\rm rms} = 0.02$

Re	control	$C_f \cdot 10^2$	$\mathrm{St}_m \cdot 10^2$	A	A_{net}	U_p	$\langle\phi\rangle_{\rm rms}/\phi_{\rm rms}$	grid
2293	no control	0.858	0.430	1.00	–	–	–	Case 1
	suboptimal	1.46	0.882	1.21	1.31	0.380	0.804	Case 1
	open-loop	1.46	0.840	1.15	1.25	0.380	–	Case 1
5055	no control	0.703	0.357	1.02	–	–	–	Case 4
	suboptimal	1.28	0.767	1.20	1.26	0.417	0.654	Case 4
	open-loop	1.13	0.629	1.11	1.17	0.417	–	Case 4
8034	no control	0.631	0.323	1.02	–	–	–	Case 5
	suboptimal	1.29	0.777	1.20	1.27	0.454	0.704	Case 5
	open-loop	1.13	0.649	1.15	1.21	0.454	–	Case 5

4.4. *Reynolds number effects*

Although detailed discussions on Reynolds number effects in the dissimilar control are out of the scope of the present paper, we briefly show control results at two higher Reynolds numbers, i.e., Re = 5055 and 8034, which correspond to the friction Reynolds numbers of $\mathrm{Re}_\tau = 300$ and 450 in the cases of uncontrolled flows, respectively. The amplitude of the control input is kept constant as $\phi_{rms} = 0.02$ and the same computational domain, i.e., $(L_x, L_z) = (2.5\pi, \pi)$ is used in all cases. The details of numerical conditions are shown in Table 1.

In all Reynolds numbers, similar traveling wave-like control inputs are obtained. The conditionally-averaged control inputs $\langle\phi\rangle$ at different Reynolds numbers are shown in Fig. 10. It is found that wall blowing decays more gradual in the upstream of the maximum-wall-blowing location at higher Reynolds numbers, while the profiles in the downstream are almost independent of the Reynolds number.

The control performance and the features of the control input are summarized in Table 4. The data of the uncontrolled flow are also listed for comparison. At higher Reynolds numbers of 5055 and 8034, C_f and St_m in the controlled flows are almost constant, so that A and A_{net} are independent of Re within the range considered here. We also note that the phase speed U_p is slightly increased with increasing Re. The present results imply that the Reynolds number effects on the control input distribution and the resultant control performance are not remarkable.

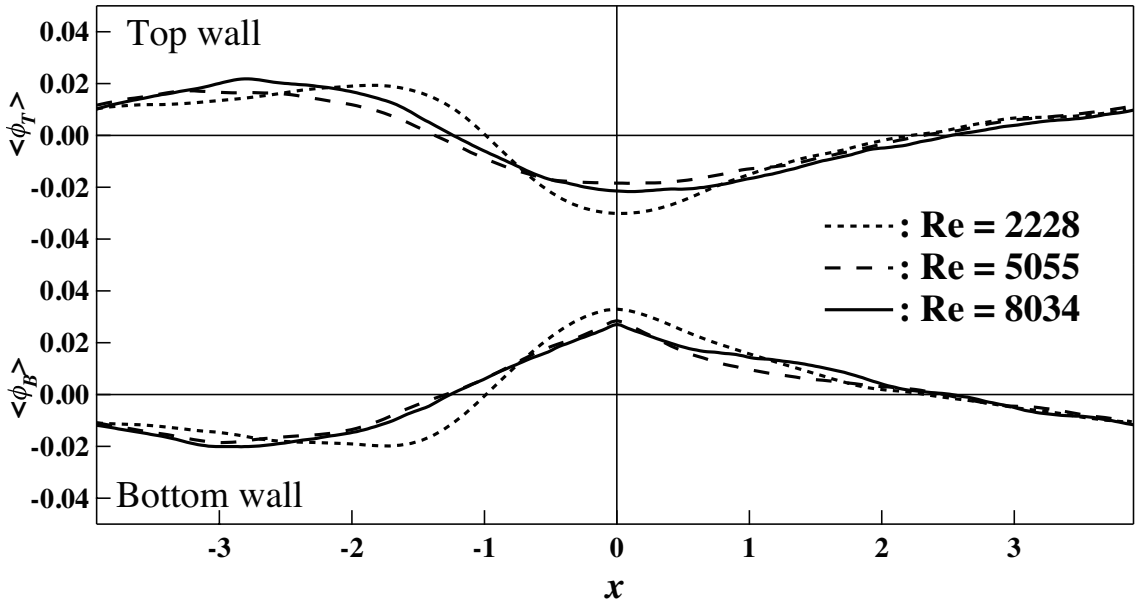

FIGURE 10. Conditionally-averaged control inputs $\langle\phi\rangle$ at the top and bottom walls for different Reynolds numbers at $\phi_{\rm rms} = 0.02$.

5. Mechanisms of Dissimilarity

5.1. *Fundamental statistics*

The mean velocity and temperature profiles in the uncontrolled and controlled flows at Re = 2293 are shown in Fig. 11. Only the results at $\phi_{\rm rms} = 0.05$ are plotted, since the general trend is similar in other cases with different amplitudes of control input. In the uncontrolled flow, the profiles of $\overline{u}$ and $\overline{\theta}$ are almost identical. However, the curvature of the mean temperature in the central region of the channel is slightly smaller than that of the mean velocity. We confirmed that this small deviation still remains in a calculation with finer grid resolution. This implies slightly better mixing for temperature in the central part of the channel even in the uncontrolled flow, but causes little change of A from unity (see, Table 2). This is because the turbulence contribution to St_m or C_f is much smaller in the central region than that near the wall as suggested by Eqs. (2.13) and (2.14).

When the dissimilar control is applied, both gradients of the mean velocity and temperature at the wall are larger than those in the uncontrolled flow. This results in the increase of friction drag and heat transfer. With the distance from the wall, both the mean velocity and temperature once become smaller than those in the uncontrolled flow at 0.1δ–0.5δ, and then much larger in the central region. This modification is more pronounced in the temperature profile. As will be discussed later, they are attributed to the traveling wave-like control input.

The shear stress and heat flux distributions in the uncontrolled and controlled flows at $\phi_{rms} = 0.05$ are shown in Fig. 12. The shear stress is composed of the viscous stress $(1/\mathrm{Re})d\overline{u}/dy$ and the Reynolds stress $-\overline{u'v'}$, whereas the heat flux has similar contributions from the molecular heat flux $(1/\mathrm{Re})d\overline{\theta}/dy$ and the turbulent heat flux $-\overline{\theta'v'}$. Since both the mean pressure gradient and the heat source in Eqs. (2.5) and (2.6) are uniform throughout the channel, the total stress and flux should be linearly distributed in the y direction. In the uncontrolled flow, both distributions almost coincide, and this suggests the strong similarity between momentum and heat transfer. In the controlled flow, the turbulent heat flux is more enhanced than the Reynolds shear stress, although both of

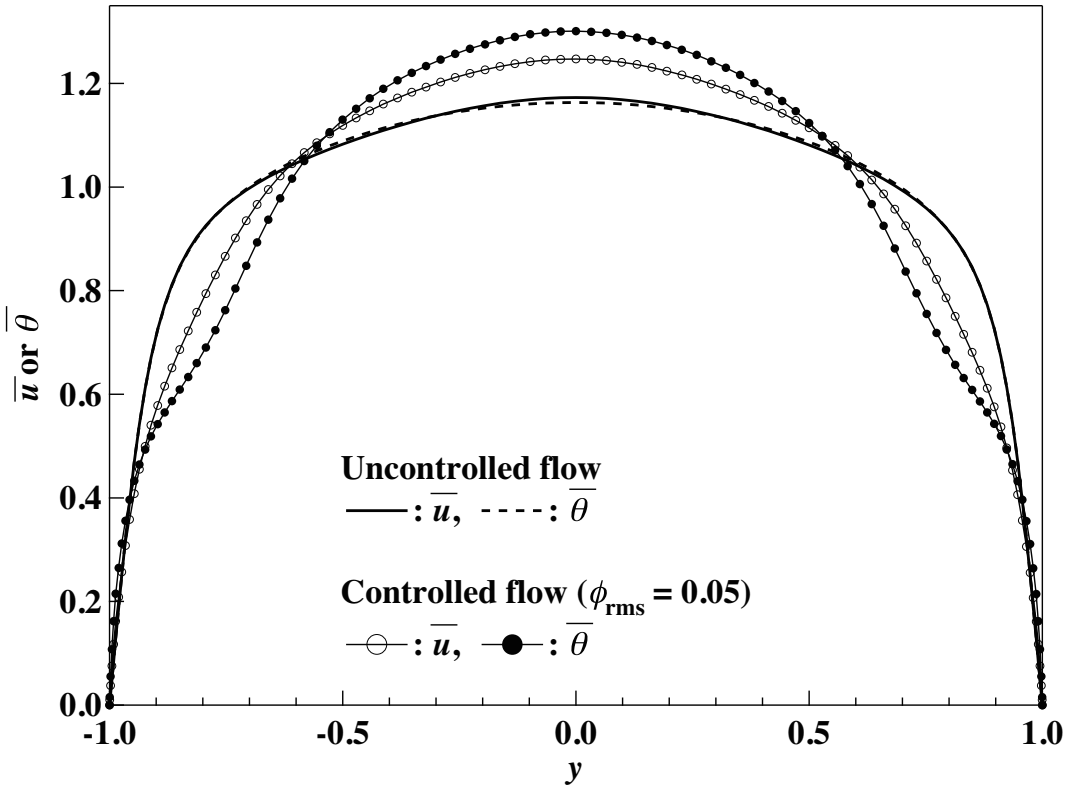

FIGURE 11. Mean velocity and temperature profiles in uncontrolled and control flows at $\phi_{\mathrm{rms}} = 0.05$

them are increased beyond those in the uncontrolled flow. Note that the stress and heat flux at the wall in Fig. 12 correspond to $C_f/2$ and St_m, respectively. As shown in Figs. 11 and 12, statistical quantities in the controlled flow are generally symmetric with respect to the channel center due to the symmetric nature of the applied control input. Hence, we hereafter will show results only in the lower half of the computational domain, i.e., $-1 < y < 0$, unless otherwise stated.

5.2. *Decomposition of instantaneous velocity and temperature fields*

In accordance with the decomposition of the control input ϕ defined by Eq. (4.1), the instantaneous velocity and temperature in the controlled flow can also be expressed as:

$$\begin{aligned} c(x,y,z,t) &= \langle c \rangle (x - x_p, y) + c''(x - x_p, y, z, t) \\ &= \overline{c}(y) + \tilde{c}(x - x_p, y) + c''(x - x_p, y, z, t), \end{aligned} \tag{5.1}$$

where c denotes an arbitrary quantity such as velocity components, pressure and temperature. A conditionally-averaged quantity with angle brackets is further decomposed into mean and coherent components represented by an over-bar and a tilde, respectively.

By applying the decomposition defined by Eq. (5.1), the Reynolds stress $\overline{u'v'}$ and the turbulent heat flux $\overline{\theta'v'}$ in Eqs. (2.13) and (2.14) can be further decomposed as follows:

$$C_f = \frac{6}{\mathrm{Re}} + 3\int_{-1}^{1} y\left\{\overline{\tilde{u}\tilde{v}} + \overline{u''v''}\right\} dy, \tag{5.2}$$

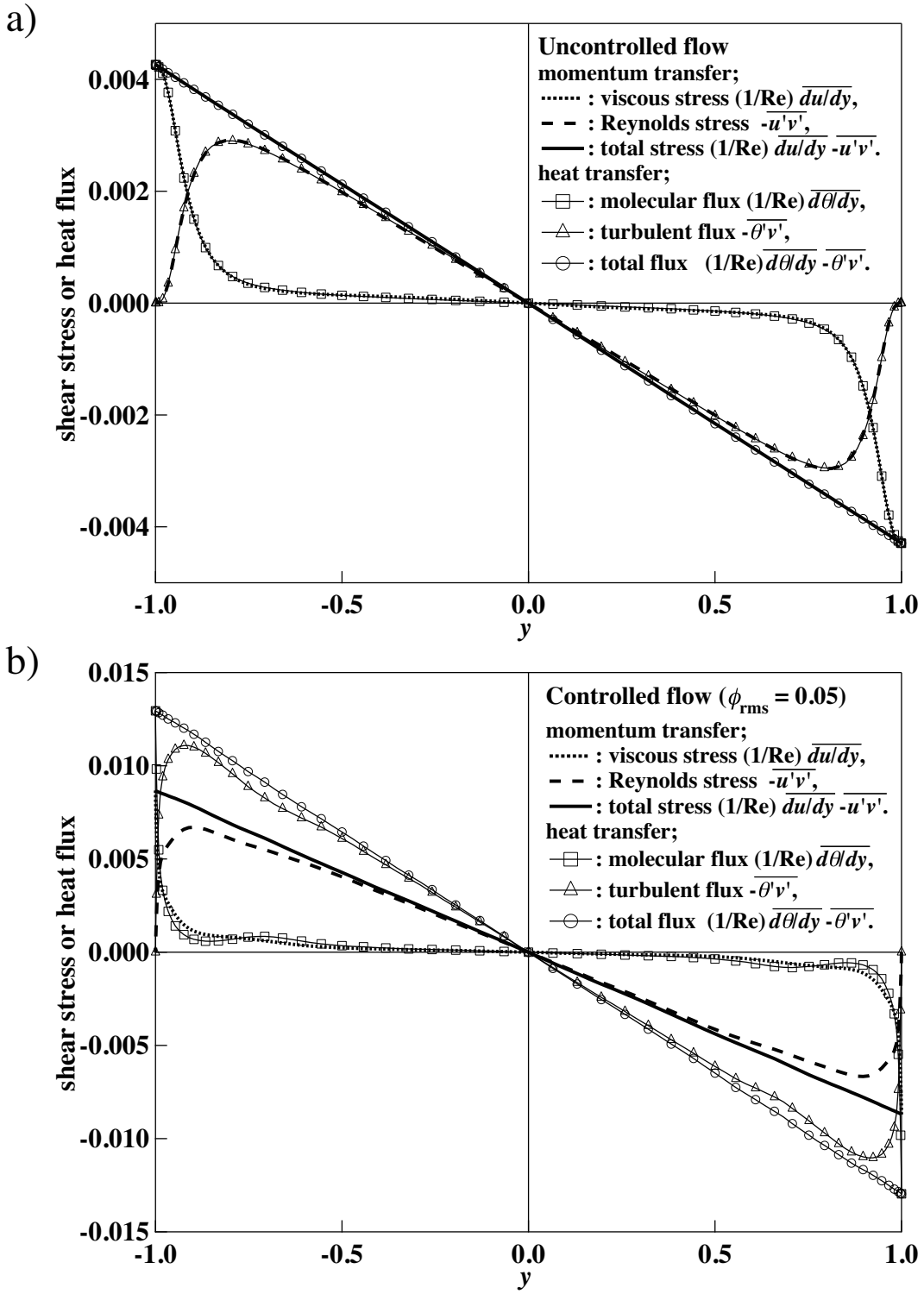

FIGURE 12. Turbulent shear stress and heat flux in a) uncontrolled and b) controlled flows at $\phi_{\rm rms} = 0.05$.

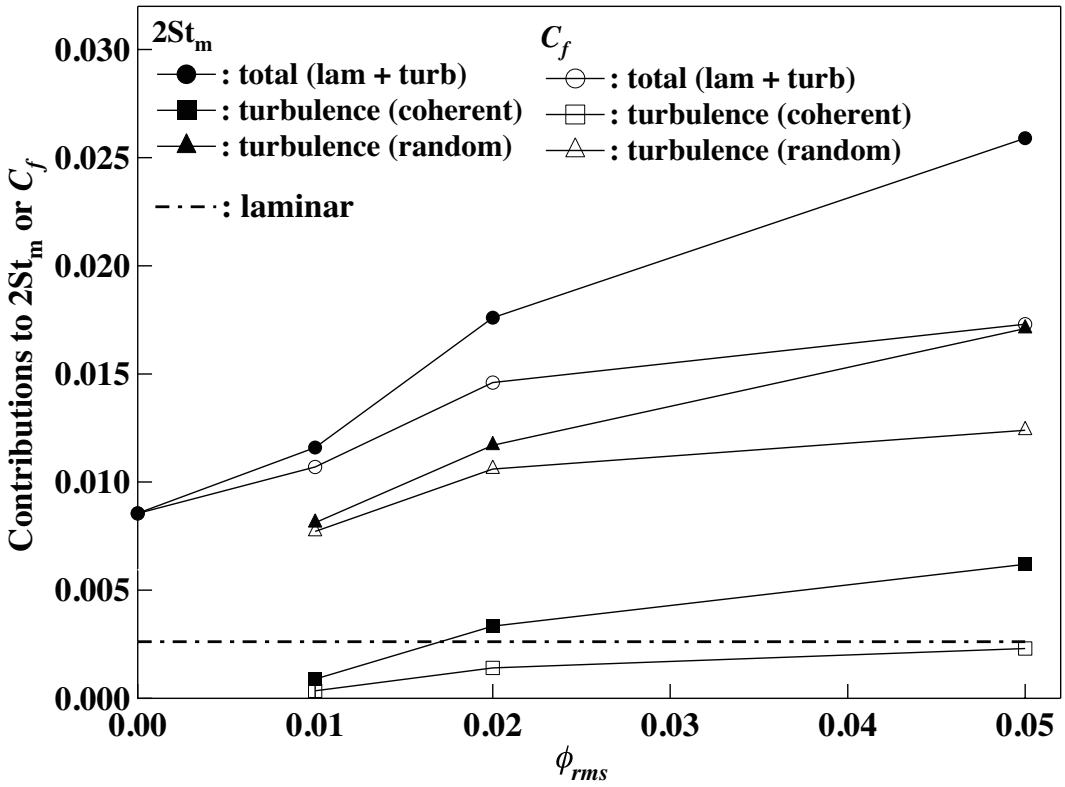

FIGURE 13. Laminar and turbulence contributions to $2\mathrm{St}_m$ and C_f for different amplitudes of the control input.

$$2\mathrm{St}_m = \frac{6}{\mathrm{Re}} + 3\int_{-1}^{1} y\left\{\overline{\tilde{\theta}\tilde{v}} + \overline{\theta'' v''}\right\} dy. \tag{5.3}$$

The laminar contributions on the right hand side of these equations are identical and constant regardless of the control. The first term in the integrand represents the contribution from the coherent mode, while the second from the random fluctuations.

In Fig. 13, the contributions from the coherent and random components to $2\mathrm{St}_m$ and C_f at different amplitudes of control input are shown. The laminar contribution is depicted by a dashed-dotted line, whereas the total (laminar + turbulence) contributions to $2\mathrm{St}_m$ and C_f by solid and open circles, respectively. Note that $\phi_{rms} = 0$ correspond to the uncontrolled flow. With increasing the amplitude of control, the total contribution to $2\mathrm{St}_m$ increases more rapidly than that of C_f. Thus, A becomes larger than unity. Since the laminar contribution remains constant, the dissimilarity is caused by dissimilarity in the turbulence contribution. Considering the fact that the control input is dominated by the coherent component, which accounts for about 70 % of the control input as shown in Table 2, it is surprising that the contribution from the random component to dissimilarity is comparable to that from the coherent component. Actually, the contribution of the random component to dissimilarity exceeds that of the coherent component at $\phi_{rms} = 0.05$. It should be also noted that the amplitude of the control input is generally small in the present study, i.e., $\phi_{rms} \leq 0.05$, and therefore the intensity of the induced coherent field is smaller than that of the random field. This can be seen in Fig. 13, where the random field contributes to $2\mathrm{St}_m$ and C_f much more than the coherent field. Considering this fact, it can also be said that the coherent component causes significant dissimilarity in spite of its small intensity.

In order to clarify contributions to dissimilarity at different locations from the wall,

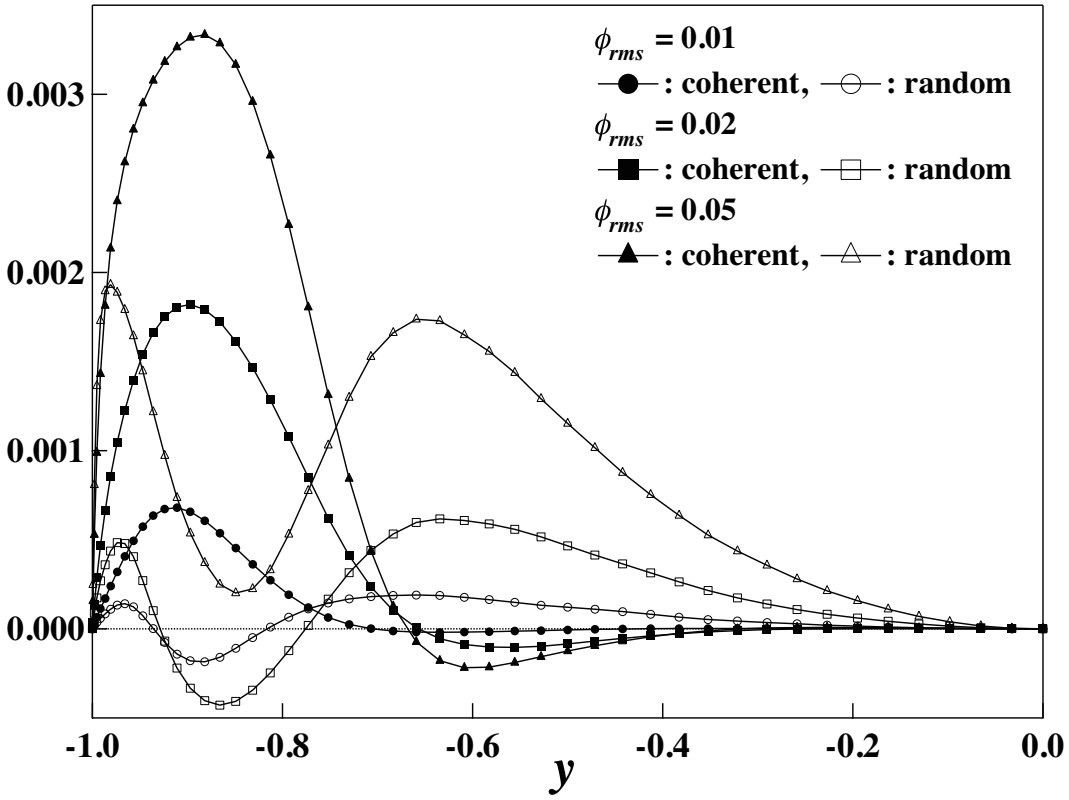

FIGURE 14. Difference between the weighted turbulent heat flux and the weighted Reynolds shear stress at different amplitudes of the control input (the coherent and random components, i.e., $y(\overline{\tilde{\theta}\tilde{v} - \tilde{u}\tilde{v}})$ and $y(\overline{\theta'' v'' - u'' v''})$, are plotted separately).

the differences between the weighted turbulent heat flux and the weighted Reynolds stress in the coherent and random components $y(\overline{\tilde{\theta}\tilde{v} - \tilde{u}\tilde{v}})$ and $y(\overline{\theta'' v'' - u'' v''})$ are plotted in Fig. 14. It is found that $y(\overline{\tilde{\theta}\tilde{v} - \tilde{u}\tilde{v}})$ has a peak in the near wall region around $y/\delta = -0.9$ and it is monotonically increased with increasing ϕ_{rms}. On the other hand, $y(\overline{\theta'' v'' - u'' v''})$ has two peaks in the vicinity of the wall, $y \approx -0.95$, and also far away from the wall, $y \approx -0.6$. In the following, we will discuss the causes for these peaks.

5.3. *Dissimilarity in the coherent component*

The conditionally-averaged streamwise velocity $\langle u \rangle$ and temperature $\langle \theta \rangle$ at $\phi_{rms} = 0.05$ are plotted in Figs. 15 a) and b). High velocity and temperature regions, i.e., $\langle u \rangle, \langle \theta \rangle > 1.0$ are depicted with solid lines, while low velocity and temperature regions i.e., $\langle u \rangle, \langle \theta \rangle < 0.5$ with dotted-lines. It is found that the responses of the velocity and temperature fields to the control input are totally different. In the central region of the channel, $\langle u \rangle$ is gradually decelerated upstream of the wall blowing, and then suddenly accelerated over the wall blowing, whereas $\langle \theta \rangle$ is hardly influenced by the wall blowing and is almost uniform in the streamwise direction. On the other hand, the abrupt wall blowing induces a low-temperature region in the downstream of the wall blowing, i.e., $0 < x < 2$, which penetrates further into the bulk region.

The conditionally-averaged wall-normal velocity $\langle v \rangle$ and pressure $\langle p \rangle$ are also plotted in Figs. 15 c) and d). Note that the mean pressure gradient is subtracted from $\langle p \rangle$. The wall-normal velocity $\langle v \rangle$ reaches its maximum around 0.25δ away from the wall above the wall blowing. This peak location is found to be almost independent of the amplitude

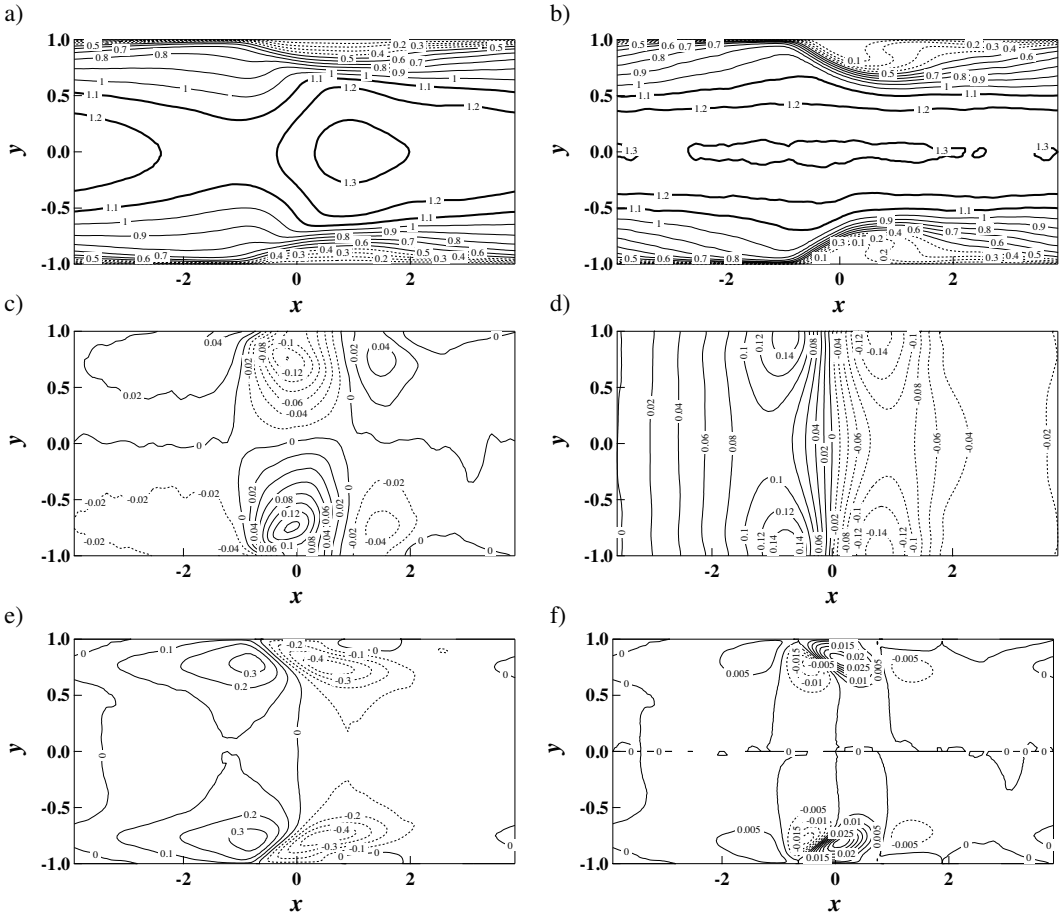

FIGURE 15. Conditionally-averaged quantities around the wall blowing at $\phi_{rms} = 0.05$. a) streamwise velocity $\langle u \rangle$, b) temperature $\langle \theta \rangle$, c) wall-normal velocity $\langle v \rangle$, d) pressure $\langle p \rangle$, e) difference between the phase fluctuations of temperature and streamwise velocity $\tilde{\theta} - \tilde{u}$, f) difference between the weighted turbulent heat flux and Reynolds stress arising from coherent compoents $y(\tilde{\theta}\tilde{v} - \tilde{u}\tilde{v})$. In a) and b), high velocity and temperature regions, i.e., $\langle u \rangle, \langle \theta \rangle > 1.0$ are depicted with thick lines, while low velocity and temperature regions, i.e., $\langle u \rangle, \langle \theta \rangle < 0.5$ with dotted lines. In c) - f), positive regions are depicted with solid lines, while negative regions with dotted lines. In all figures, the vertical scale is doubled so as to make near-wall profiles visible.

of the control input (not shown here). The wall blowing generates significant positive and negative pressure fluctuations in its upstream and downstream regions, respectively. Similar results are also reported by Kong et al. (2001), who applied wall blowing through a spanwise slot in a turbulent boundary layer.

In Figs. 15 e), the difference between the coherent components of temperature and streamwise velocity, i.e., $\tilde{\theta} - \tilde{u}$, is plotted. Upstream of the abrupt wall blowing, $\tilde{u}$ is generally smaller than $\tilde{\theta}$ due to adverse pressure gradient induced by the wall blowing as shown in Fig. 15 d). In contrast, above the wall blowing region, strong favorable pressure gradient accelerates $\tilde{u}$, and eventually $\tilde{u}$ exceeds $\tilde{\theta}$ in the downstream region. The difference between the weighted turbulent heat flux and Reynolds stress, i.e., $y(\tilde{\theta}\tilde{v} - \tilde{u}\tilde{v})$ is plotted in Fig. 15 f). Note that $\tilde{v}$ is identical to $\langle v \rangle$ shown in Fig. 15 c), since $\overline{v} = 0$. A region with large positive $y(\tilde{\theta}\tilde{v} - \tilde{u}\tilde{v})$ is confirmed just above the abrupt wall blowing, where $\langle u \rangle$ is substantially accelerated by the favorable pressure gradient. This causes the prominent peak of $y(\overline{\tilde{\theta}\tilde{v} - \tilde{u}\tilde{v}})$ near the wall shown in Fig. 14.

We also plot the eddy diffusivities for momentum and heat, i.e., $\tilde{E}_v$ and $\tilde{E}_c$ for the

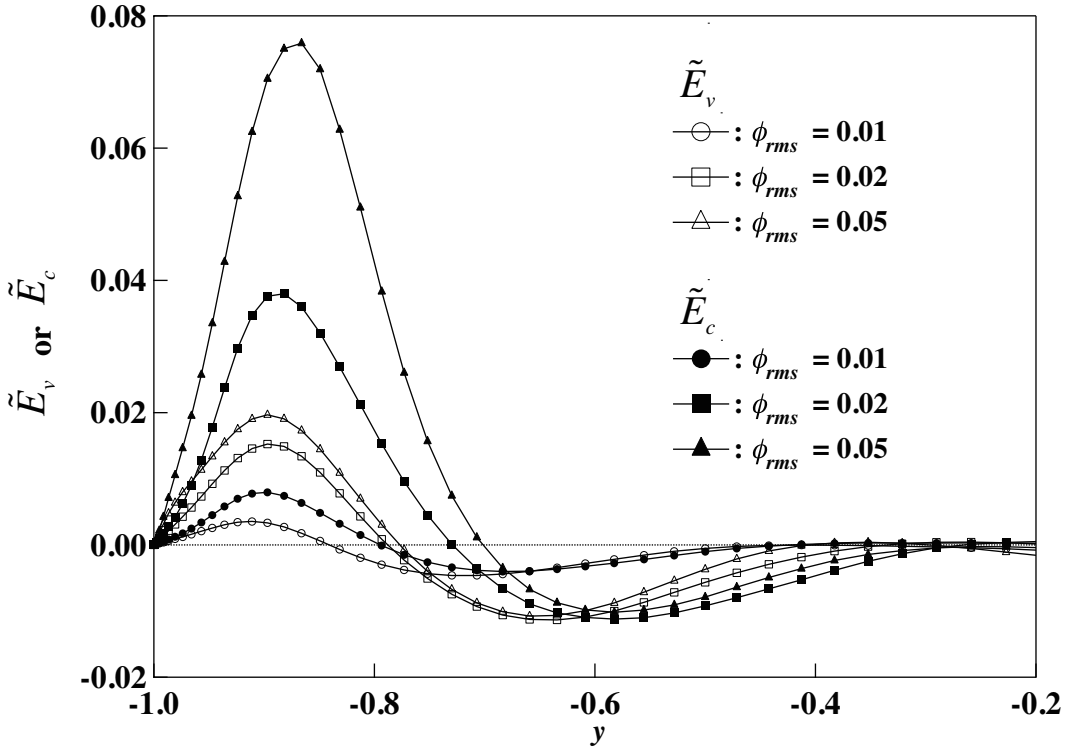

FIGURE 16. The eddy diffusivities for momentum $\tilde{E_v}$ and heat $\tilde{E_c}$ for the coherent components.

coherent components in Fig. 16. Here, $\tilde{E_v}$ and $\tilde{E_c}$ are respectively defined as:

$$\tilde{E_v} = \frac{-\overline{\tilde{u}\tilde{v}}}{\left(\dfrac{d\overline{u}}{dy}\right)}, \quad \tilde{E_c} = \frac{-\overline{\tilde{\theta}\tilde{v}}}{\left(\dfrac{d\overline{\theta}}{dy}\right)}. \tag{5.4}$$

It is observed that $\tilde{E_c}$ is more enhanced than $\tilde{E_v}$ at around $y = -0.9$ and this agrees well with the peak location of $y(\overline{\tilde{\theta}\tilde{v}} - \overline{\tilde{u}\tilde{v}})$ shown in Fig. 14. Consequently, the inverse of the turbulent Prandtl number for the coherent components reaches $\tilde{\mathrm{Pr}}_t^{-1} = \tilde{E_c}/\tilde{E_v} \approx 4$ around the peak location. These results imply that the local turbulent momentum and heat transfer mechanisms are made dissimilar by the traveling wave-like control input.

5.4. *Dissimilarity in the random component*

Since the mean velocity and temperature profiles in the controlled flow are no longer similar (see, Fig. 11), the dissimilarity between turbulent heat and momentum transport in the random component should be discussed through comparison between the eddy diffusivities for momentum E_v'' and heat E_c'', rather than $\overline{u''v''}$ and $\overline{\theta''v''}$ themselves. We define these quantities in the controlled flow as follows:

$$E_v'' = \frac{-\overline{u''v''}}{\left(\dfrac{d\overline{u}}{dy}\right)}, \quad E_c'' = \frac{-\overline{\theta''v''}}{\left(\dfrac{d\overline{\theta}}{dy}\right)}. \tag{5.5}$$

As a result, the difference between $\overline{\theta''v''}$ and $\overline{u''v''}$ is expressed as follows:

$$\overline{\theta''v''} - \overline{u''v''} = (\mathrm{Pr}''^{-1}_t S - 1)\overline{u''v''}. \tag{5.6}$$

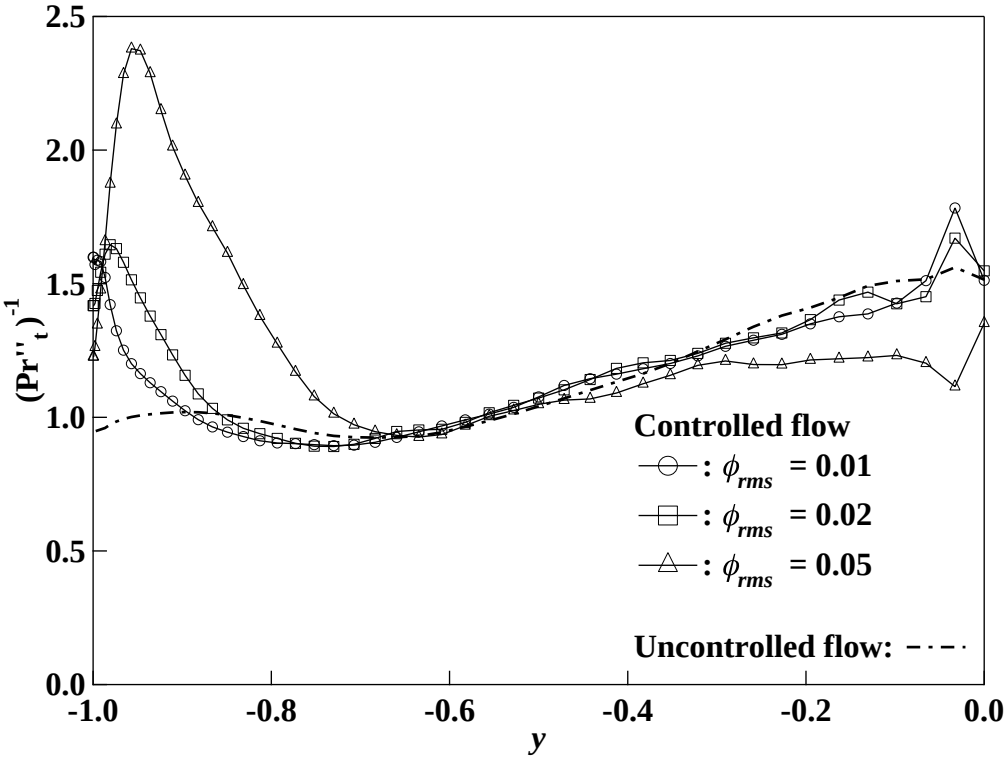

FIGURE 17. Inverse of turbulent Prandtl number Pr''^{-1}_t for the random components in uncontrolled and controlled flows.

Here, S is the ratio of the mean temperature gradient and the mean velocity gradient, $S = (d\overline{\theta}/dy)/(d\overline{u}/dy)$. The turbulent Prandtl number is defined as $\mathrm{Pr}''_t = E''_v/E''_c$. The above equation indicates that the dissimilarity between $\overline{\theta''v''}$ and $\overline{u''v''}$ is caused by enhancement of either Pr''^{-1}_t or S.

In Fig. 17, the profiles of Pr''^{-1}_t at different amplitudes of control input are presented. The data of uncontrolled flow are also shown for comparison. It is found that Pr''^{-1}_t is monotonically increased with increasing ϕ_{rms} in the near-wall region, while it is almost unchanged or even slightly decreased far from the wall at $y > -0.6$. It is interesting to note that Pr''^{-1}_t becomes larger than unity even in the uncontrolled flow away from the wall. This is consistent with the slight difference between the mean velocity and temperature profiles in the channel central region shown in Fig. 11. We found that the streamwise velocity fluctuation becomes totally smaller than the temperature fluctuation in this region (not shown here). This can be attributed to the pressure strain effect, which redistributes the streamwise velocity fluctuation to the other two components.

The profiles of S are also plotted in Fig. 18. It is found that S exceeds unity in the very vicinity of the wall, whereas it first decreases rapidly with increasing the distance from the wall, and then becomes larger than the value of the uncontrolled flow again further away from the wall. Note that the limiting value of S at the wall should be identical to A. From Figs. 17 and 18, we conclude that the two peaks of $y(\overline{\theta''v''} - \overline{u''v''})$ observed in Fig. 14 are caused by different mechanisms, namely, the first peak near the wall is attributed to the increase in Pr''^{-1}_t, whereas the second peak away from the wall to the increase in S. As will be shown in Sec. 6, the increase in Pr''^{-1}_t near the wall is caused by the random component ϕ'' of the control input.

In order to explain the increase of S in the central region of the channel, we revisit

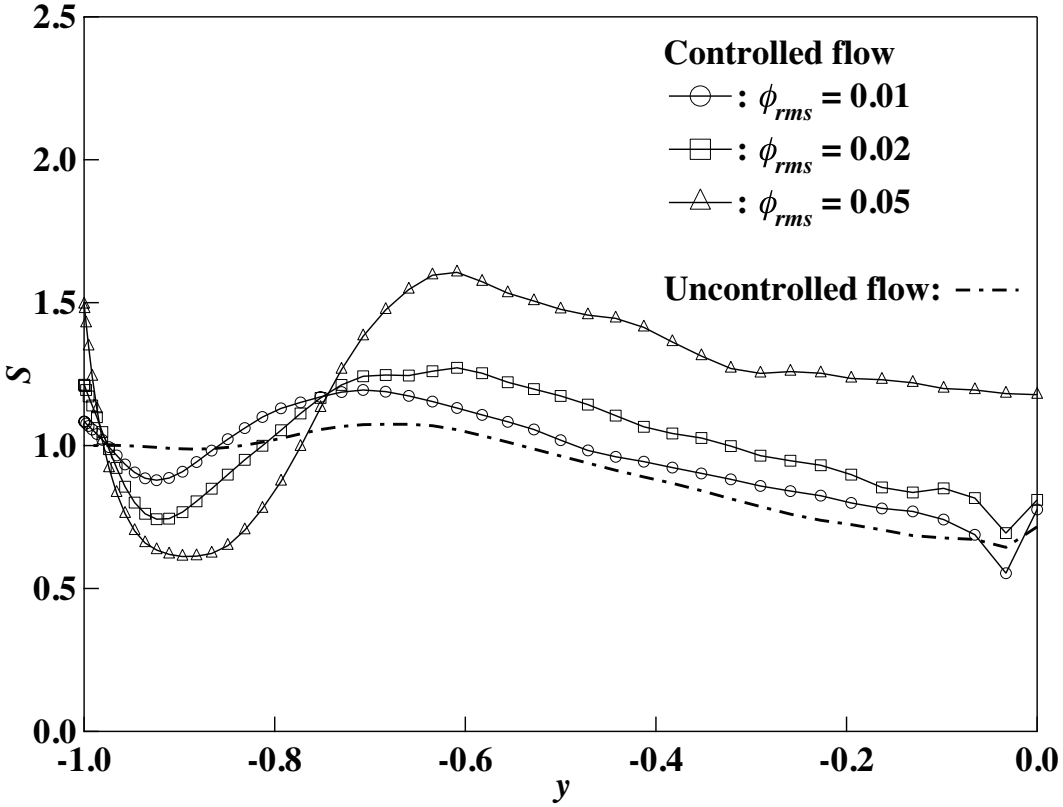

FIGURE 18. Ratio of the mean temperature gradient $d\overline{\theta}/dy$ and the mean velocity gradient $d\overline{u}/dy$ in uncontrolled and controlled flows.

the averaged momentum and energy transport equations of Eqs. (2.5) and (2.6), where the wall-normal derivatives of the Reynolds stress and the turbulent heat flux diffuse the mean velocity and temperature within the channel. In Fig. 19, these two derivatives arising from the coherent velocity and thermal fields, $-\partial(\overline{\tilde{u}\tilde{v}})/\partial y$ and $-\partial(\overline{\tilde{\theta}\tilde{v}})/\partial y$, at $\phi_{rms} = 0.05$ are plotted. The mean pressure gradient $-d\overline{p}/dx$ and the heat source term Q, which are uniform across the channel, are also presented for comparison.

It is found that the magnitudes of $-\partial(\overline{\tilde{u}\tilde{v}})/\partial y$ and $-\partial(\overline{\tilde{\theta}\tilde{v}})/\partial y$ are comparable to the mean pressure gradient and the heat source. In addition, they change substantially from high values near the wall to the minimum peaks, and then approaching to zero at the channel center. This indicates that the coherent velocity and thermal fields induced by the traveling wave-like input transfer the mean streamwise momentum and heat from a region slightly away from the wall to the near-wall and central regions of the channel. This effect can clearly be observed in Figs. 11, where the mean velocity and temperature in controlled flow are significantly lower than those of uncontrolled flow slightly away from the wall, while increased in the near-wall and central regions of the channel. Since the above effect is more pronounced in the thermal field (see, Fig. 19), the mean temperature gradient becomes steeper than the mean velocity gradient in the central regions of the channel. The above results indicate that the second peak of $y(\overline{\theta'' v''} - \overline{u'' v''})$ away from the wall shown in Fig. 14 is caused by the indirect effect of the coherent fluctuations through modification of the mean velocity and temperature profiles.

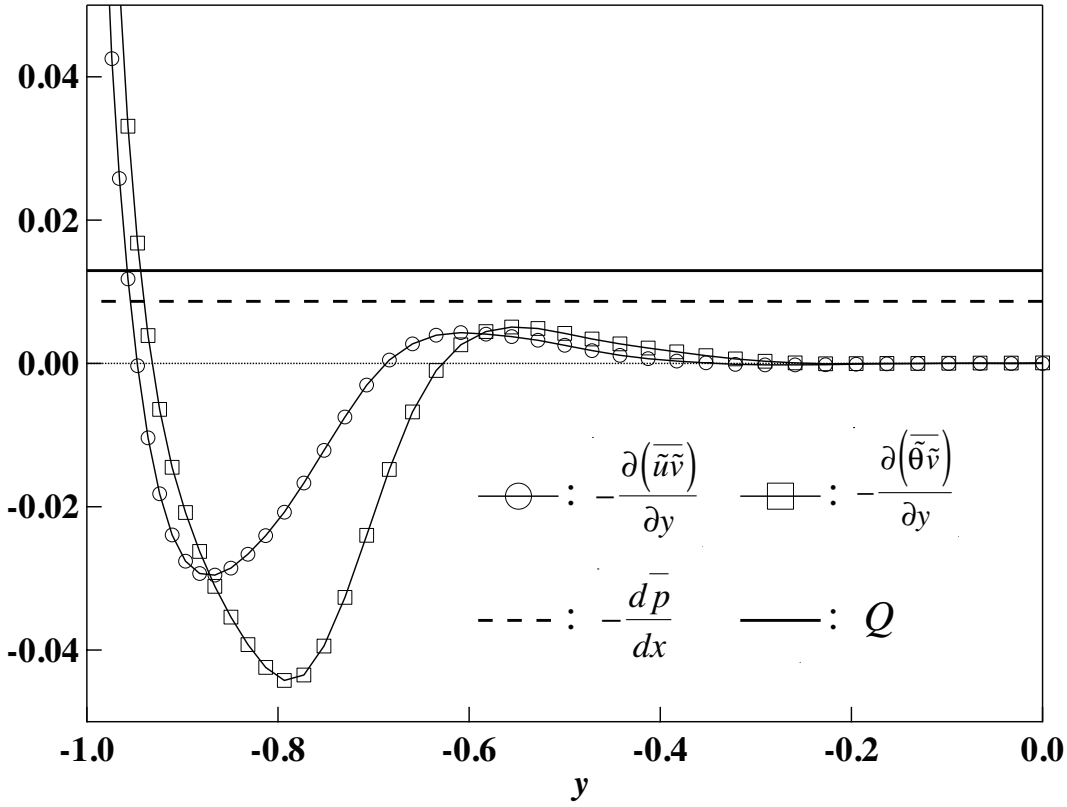

FIGURE 19. Wall normal gradients of the Reynolds stress and the turbulent heat flux arising from the coherent component at $\phi_{rms} = 0.05$.

6. Open-loop dissimilar control

6.1. *Numerical procedure*

We have shown that the traveling wave-like control input causes dissimilarity between $2\mathrm{St}_m$ and C_f through two different mechanisms, namely, the direct modification of the coherent velocity and thermal fields, $y(\overline{\tilde{\theta}\tilde{v} - \tilde{u}\tilde{v}})$, and the indirect effect on the random fields, $y(\overline{\theta'' v'' - u'' v''})$, through modification of the mean velocity and temperature profiles. Following these results, we design additional numerical simulations, in which the profile of the control input and its phase speed are prescribed by referring to the coherent control input obtained in the suboptimal control. The significance of such computations is as follows. First, the achievement of dissimilarity by a simple open-loop strategy provides a more practical pathway for real applications. Second, we can validate the above-mentioned mechanism of dissimilar heat transfer enhancement. Third, we can systematically assess the effects of the phase speed on control performance.

The wave-form of the open-loop control input is taken from the coherent component $\langle\phi\rangle$ of the suboptimal control input at $\phi_{rms} = 0.05$ shown in Fig. 7. The phase speed obtained by the suboptimal control is $U_p = 0.277$ in Table 2, but it is changed as $U_p = -0.554, -0.277, 0, 0.277, 0.554, 0.831$ and 1.11. In all cases, the same grid system as Case 1 is employed.

6.2. *Control performance*

The control results obtained by the present open-loop control is summarized in Table 5. It is found that both C_f and St_m become maximum when the phase speed is about

TABLE 5. Control results of open-loop control with different phase speed U_p

U_p	$C_f \cdot 10^2$	$\mathrm{St}_m \cdot 10^2$	A	A_{net}	ϕ_{rms}
-0.554	1.07	0.596	1.11	1.15	0.033
-0.277	1.29	0.740	1.15	1.20	0.033
0	1.53	0.929	1.22	1.30	0.033
0.277	1.83	1.19	1.30	1.43	0.033
0.554	2.07	1.32	1.27	1.47	0.033
0.831	1.49	0.769	1.03	1.07	0.033
1.11	1.02	0.513	1.01	1.00	0.033
(suboptimal)	1.74	1.31	1.51	1.61	0.050
(no control)	0.858	0.430	1.00	–	–

the half of the bulk mean velocity, i.e., $U_p = 0.554$. It should be noted, however, that A is most enhanced when the phase speed coincides with the value obtained in the suboptimal control, $U_p = 0.277$. This is not obvious, since the suboptimal control theory takes into account only the short-time flow dynamics, and therefore does not ensure that the resultant control input is optimal in a long time horizon.

It is also found that A obtained by the open-loop control is commonly smaller than that obtained by the suboptimal control. In the present open-loop control, only the coherent component $\langle\phi\rangle$ of the suboptimal control input is applied, so that the deterioration of the control performance should be attributed to the absence of the random component ϕ''. We also note that the amplitude of the control input, i.e., ϕ_{rms} in the open-loop control is smaller by 34 % than that of the corresponding suboptimal control input due to the absence of ϕ'' (see, Table 5). Although the control performances of the present open-loop control cannot reach those of the suboptimal control, it should be emphasized that dissimilar control is achieved by such a simple algorithm with small control input.

In Fig. 20, $y(\overline{\tilde{\theta}\tilde{v} - \tilde{u}\tilde{v}})$ in the open-loop control is shown. The data in the suboptimal control at $\phi_{rms} = 0.05$ are also plotted for comparison. At $U_p = 0.277$, $y(\overline{\tilde{\theta}\tilde{v} - \tilde{u}\tilde{v}})$ in the open-loop control agrees quite well with that of the suboptimal control. We also confirmed that the coherent velocity and thermal fields induced by the open-loop control are quite similar to those by the suboptimal control, when the phase speed of the traveling wave-like control input is equal (not shown here). This is not obvious, since the random component of the closed-loop control input may influence the dynamics of the coherent field via nonlinear effects. These results implies that the nonlinear coupling between the coherent and random components is rather minor in the present control.

It is found that $y(\overline{\tilde{\theta}\tilde{v} - \tilde{u}\tilde{v}})$ first increases with increasing U_p up to 0.554, and then drastically decreases when U_p is further increased. We confirmed that the distributions of $\langle v\rangle$ and $\langle p\rangle$ around the localized wall blowing are almost unchanged when $U_p \leq 0.554$ (not shown here). This indicates that almost the same pressure gradient is produced at the wall blowing. Since the flow is convected downstream, the fluid particle experiences the pressure gradient for a longer period as U_p approaches to a typical convection velocity in the near-wall region. This explains why $y(\overline{\tilde{\theta}\tilde{v} - \tilde{u}\tilde{v}})$ is most enhanced at $U_p = 0.554$. This "quasi-resonance effect" also reported in previous studies by Quadrio et al. (2009) and Mamori et al. (2010). The former shows that the streamwise traveling wave control with the spanwise wall velocity causes drag increase when $0.525 < U_p < 0.75$, while the

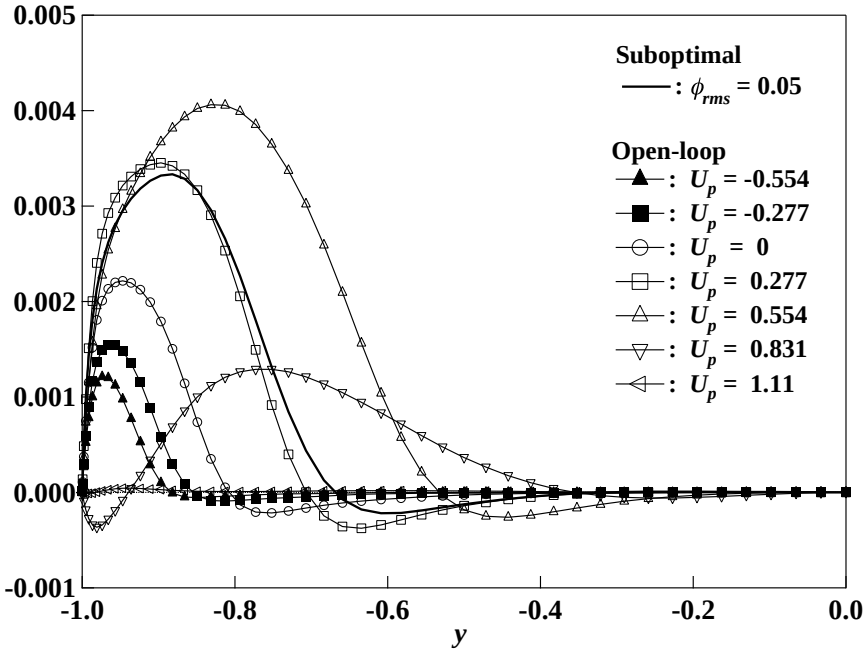

FIGURE 20. Difference between the coherent components of the weighted turbulent heat flux and the weighted Reynolds shear stress, i.e., $y(\overline{\tilde{\theta}\tilde{v} - \tilde{u}\tilde{v}})$, in the open-loop control at different phase speed U_p.

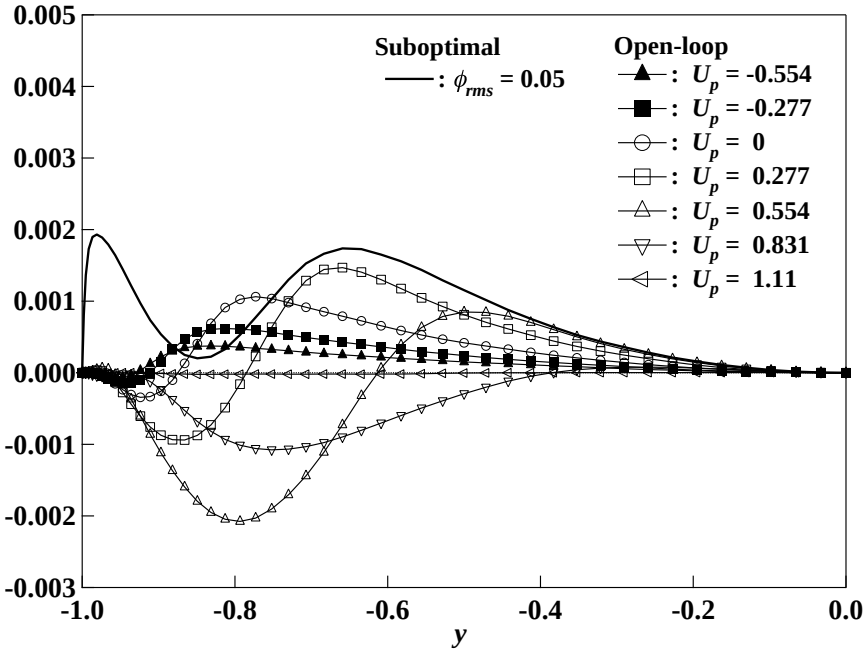

FIGURE 21. Difference between the random components of the weighted turbulent heat flux and the weighted Reynolds shear stress, i.e., $y(\overline{\theta'' v'' - u'' v''})$, in the open-loop control at different phase speed U_p.

latter performs linear analyses of a laminar channel flow subjected to the streamwise traveling wall blowing/suction and concludes that turbulence is most enhanced when $U_p \approx 0.6$. Note that C_f and St_m become maximum at $U_p = 0.554$ in the present control (see, Table 5).

In contrast to $y(\overline{\tilde{\theta}\tilde{v} - \tilde{u}\tilde{v}})$, $y(\overline{\theta'' v'' - u'' v''})$ shows different dependency on U_p as shown in Fig. 21. Specifically, negative contribution becomes more dominant near the wall with increasing U_p. This causes the decrease in A at $U_p \geq 0.544$. It is also found that $y(\overline{\theta'' v'' - u'' v''})$ in the open-loop control at $U_p = 0.277$ agrees fairly well with that in the suboptimal control far from the wall, whilst the positive peak near the wall disappears in the open-loop control. As discussed in Eq. (5.6), the first peak of $y(\overline{\theta'' v'' - u'' v''})$ near the wall is attributed to increase in ${\mathrm{Pr}''_t}^{-1}$. Actually, the prominent peak of ${\mathrm{Pr}''_t}^{-1}$ observed in the suboptimal control no longer exists in the open-loop control (not shown here). This indicates that the random component ϕ'' of the control input, which is present only in the suboptimal control, causes the increase of ${\mathrm{Pr}''_t}^{-1}$ in the near-wall region. This explains why A achieved in the open-loop control is commonly lower than that achieved in the suboptimal control. We also found that ${\mathrm{Pr}''_t}^{-1}$ in the open-loop control does not strongly depend on U_p so that the variation of $y(\overline{\theta'' v'' - u'' v''})$ shown in Fig. 21 is mainly governed by that of S. Especially, substantial negative values of $y(\overline{\theta'' v'' - u'' v''})$ away from the wall at $U_p \geq 0.554$ are caused by significant decrease of S from unity (not shown here).

As we discussed in Fig. 19, the variation of S is caused by dissimilarity between $-\partial(\tilde{u}\tilde{v})/\partial y$ and $-\partial(\tilde{\theta}\tilde{v})/\partial y$. At $U_p = 0.554$, the coherent velocity and thermal fields are most enhanced due to the quasi-resonance effect. Although this makes $y(\overline{\tilde{\theta}\tilde{v} - \tilde{u}\tilde{v}})$ maximum (see, Fig. 20), the coherent velocity and temperature fluctuations also modifies the mean velocity and temperature gradients, and consequently causes a significant negative value of $y(\overline{\theta'' v'' - u'' v''})$ in the near-wall region. The present results indicate that the phase speed of the traveling-wave like control is optimized when it maximizes the total contribution from the direct and indirect effects in $y(\overline{\tilde{\theta}\tilde{v} - \tilde{u}\tilde{v}})$ and $y(\overline{\theta'' v'' - u'' v''})$.

6.3. *Reynolds number effects*

Finally, we discuss the Reynolds number effects on the open-loop control. Like in the previous cases, the distribution of the control input and the phase speed are determined based on the coherent component of the suboptimal control at each Reynolds number. The resultant control performances are summarized in Table 4. Similar to the suboptimal control, the Reynolds number effect in the open-loop control is generally small. Although A obtained in the open-loop control is commonly smaller than that in the suboptimal control, significant dissimilarity is achieved for all Reynolds numbers considered. In order to explore the contributions to dissimilarity, $y(\overline{\tilde{\theta}\tilde{v} - \tilde{u}\tilde{v}})$ and $y(\overline{\theta'' v'' - u'' v''})$ in the suboptimal control at different Reynolds numbers are shown in Fig. 22. With increasing Re from 2293 to 5055, $y(\overline{\tilde{\theta}\tilde{v} - \tilde{u}\tilde{v}})$ drastically decreases, and then saturates at Re = 8034. In contrast, $y(\overline{\theta'' v'' - u'' v''})$ is almost unchanged and widely-distributed throughout the channel even at higher Re. As discussed above, $y(\overline{\theta'' v'' - u'' v''})$ away from the wall is caused by the indirect effect of the traveling wave-like control input. This relative increase in the indirect effect makes the control performance almost unchanged at the higher Reynolds numbers.

7. Conclusions

Focusing on the inherent difference between the divergence-free vector and conservative scalar quantities, we demonstrate dissimilar control of momentum and heat transfer in

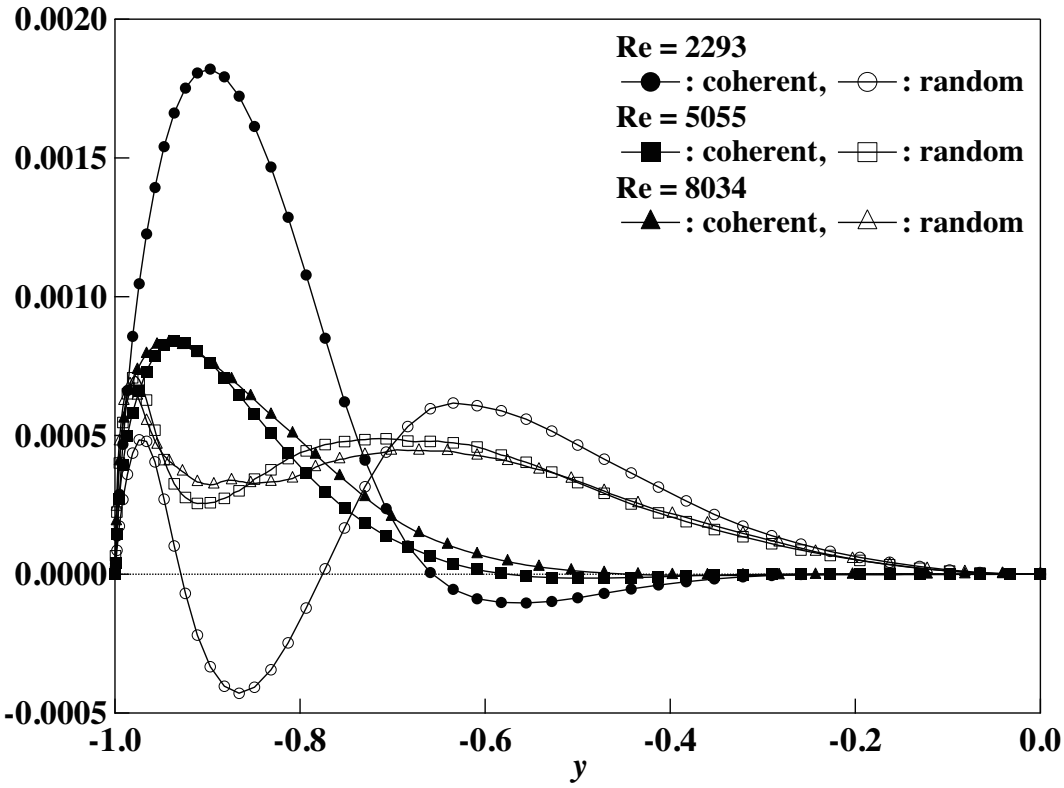

FIGURE 22. Difference between the weighted turbulent heat flux and the weighted Reynolds shear stress in the suboptimal control at different Reynolds numbers. The coherent and random components, i.e., $y(\overline{\tilde{\theta}\tilde{v}} - \overline{\tilde{u}\tilde{v}})$ and $y(\overline{\theta'' v''} - \overline{u'' v''})$ are plotted separately. For ease of identification, the symbols at Re = 5055 and 8034 are depicted every three and five grid points, respectively.

a fully developed channel flow under an ideal condition, where the averaged transport equations and the wall boundary conditions for the streamwise velocity component and the temperature are identical. The solutions of the Fréchet differentials of velocity and temperature fields clearly show that their responses to the wall blowing/suction are completely different due to the continuity constraint on the velocity field.

Although we focus on relatively small amplitudes of control input, significant control effects are observed. More specifically, St_m roughly increases by a factor of three from that of uncontrolled flow, while C_f remains doubled, when the root-mean-square value of the control input is kept 5% of the bulk mean velocity at Re = 2293. By taking into account power consumption for the control, we also show that the present control enhances heat transfer per a unit total power consumption by a factor of up to 1.85 in principle. The Reynolds number effect on the analogy factor is found to be rather week, whereas St_m increases by a factor of 2.05, 2.15 and 2.45, when the magnitude of control input is kept 2% of the bulk mean velocity at $\mathrm{Re} = 2293, 5055, 8034$, respectively. These results indicate that the present control efficiently enhances heat transfer with suppressing the total power consumption.

The obtained control input exhibits a traveling wave-like property characterized by localized wall blowing from a narrow spanwise band associated with weak suction more evenly distributed in the upstream of the blowing region. This wave is found to travel in the downstream direction at an almost constant phase speed, i.e., about $30 - 40\%$ of the bulk mean velocity. In addition, the control inputs at two opposing walls are applied in a varicose-mode. By decomposing the instantaneous velocity and temperature fields into the coherent and random fluctuations, detailed phase relationship between the traveling

wave-like control input and the velocity and thermal fields are clarified. Visualization of the coherent velocity and thermal fields show that the localized wall blowing generates significant positive and negative pressure fluctuations in its upstream and downstream regions, respectively. The favorable pressure gradient above the wall blowing accelerates the streamwise velocity, and consequently causes significant dissimilarity between the streamwise velocity component and the temperature. Note that this dissimilar effect is essentially caused by the continuity constraint on the velocity field.

The traveling wave-like control input contributes to dissimilar heat transfer enhancement through two distinct mechanisms, i.e., direct and indirect effects. The former is caused by the direct modification of the coherent velocity and thermal fields, which results in dissimilarity between the coherent components of the weighted Reynolds shear stress and the weighted turbulent heat flux. The significant increase of the inverse of the turbulent Prandtl number for the coherent component $\tilde{\mathrm{Pr}}_t^{-1}$ near the wall indicates that the turbulent heat and momentum transport mechanisms are made dissimilar by the traveling wave-like control. This effect is most pronounced when the phase speed of the traveling wave-like control input approaches about the half of the bulk mean velocity. In the meanwhile, the coherent velocity and thermal fluctuations redistribute the mean streamwise momentum and heat from a region slightly away from the wall to the near-wall and channel-central regions, and therefore modify the ratio of the mean velocity and temperature gradients. This indirectly causes dissimilarity between the random components of the weighted Reynolds shear stress and the weighted turbulent heat flux, even though the turbulent Prandtl number for the random component $\tilde{\mathrm{Pr}}''_t$ remains almost unchanged. As a result, the dissimilar heat transfer is most enhanced when the total contribution from the above two effects becomes maximum. Since the averaged, coherent and random components of the velocity and thermal fields are intrinsically coupled with each other, dissimilar effects may not be rigorously classified into the direct and indirect effects as mentioned above. Nonetheless, such classification would be helpful for understanding the dissimilar mechanisms and predicting the control performance without conducting expensive DNS in the future work.

The present study opens up a possibility to achieve dissimilar control with a simple open-loop strategy even in an extremely difficult case. Since the present study focuses on small amplitudes of the control input, more investigations with higher amplitudes are necessary to clarify how much A can be increased by the traveling wave-like control input. It is also interesting to consider how the present strategy works in more general flow conditions. Since the direct effect of the traveling wave should appear even in a laminar flow, the present strategy is expected to work in a laminar flow, where mixing enhancement with least power input is always crucial. As for higher Reynolds numbers, the present calculations imply that the direct effect is suppressed at high Reynolds numbers, whereas the indirect effect is kept almost unchanged so that the Reynolds number effect on the resultant control performance remains small. Whether this knowledge holds at further higher Reynolds numbers is still an open question. In practical flows, there exist other sources of dissimilarity, such as different thermal wall boundary conditions, Prandtl number effects, and so forth (Kasagi et al. (2011)). In order to estimate the control performance and optimize the control input under such conditions, the prediction of the coherent velocity and thermal fields induced by the traveling wave-like control input should be a key. Linear analyses like those made by Mamori et al. (2010) might be useful for this purpose. Since the suboptimal control only takes into account short-time dynamics, the present control input may not be a real optimal solution for a long time horizon. Applying the optimal control theory, e.g., Bewley et al. (2001), instead of the suboptimal control theory, to the present problem is required to clarify this issue.

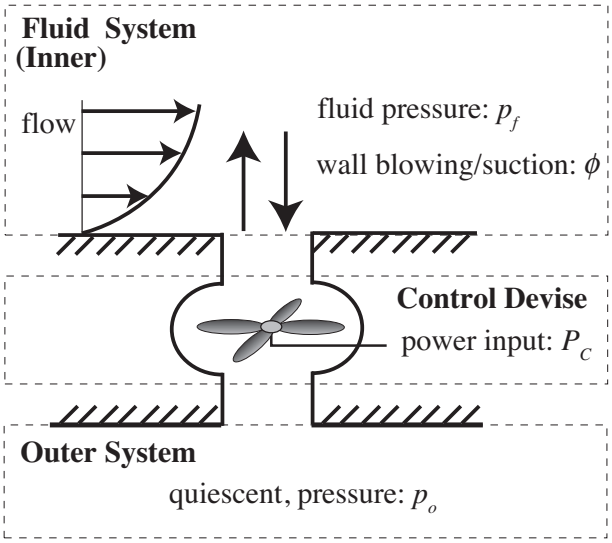

FIGURE 23. Schematic of flow control system

Acknowledgement

The authors are grateful to Dr. Koji Fukagata at Keio University and Dr. Kaoru Iwamoto at Tokyo University of Agriculture and Technology for their fruitful discussions during the course of the present work. The author (YH) greatly acknowledges the support from JSPS Postdoctoral Fellowships for Research Abroad. This work is supported by the Ministry of Education, Culture, Sports, Science and Technology of Japan (MEXT) through the Grant-in-Aid for Scientific Research (A) (No. 20246036)

Appendix A. Ideal power consumption of wall blowing/suction

Wall blowing/suction has been employed and studied in many investigations, e.g., Iwamoto et al. (2002), Min et al. (2006) and Bewley (2009). Since it inherently involves mass exchange between the flow system and the outer environment, the power consumed by actuators should depend on the thermodynamic conditions both inside and outside the flow system.

Here, we consider the ideal control power consumption for wall blowing/suction from a thermodynamic viewpoint. Figure 23 shows a schematic of flow control system. We assume that the flow (inner) system is connected to the outer system through a control devise, which can precisely control wall blowing/suction. The outer system is filled with quiescent fluid with a constant pressure p_o, and has sufficiently large capacity. The whole system is kept isothermal.

The ideal power consumption P_c for applying wall blowing/suction can be estimated by the enthalpy difference between the inner and outer systems:

$$P_c = \Delta h = (p_f - p_o)\phi + \frac{1}{2}\phi^3, \tag{A 1}$$

where p_f is the fluid pressure, which generally fluctuates in time and space. The control input ϕ is defined so that a positive value of ϕ corresponds to blowing from the wall to the fluid system. Consequently, the mean power consumption is estimated as:

$$\overline{P_c} = \overline{(p_f - p_o)\phi} + \frac{1}{2}\overline{\phi^3} = (\overline{p_f} - p_o)\overline{\phi} + \overline{p'_f\phi'} + \frac{1}{2}(\overline{\phi}^3 + 3\overline{\phi}\cdot\overline{\phi'^2} + \overline{\phi'^3}). \tag{A 2}$$

In the case of uniform blowing/suction from the wall, ϕ' vanishes and $\phi = \overline{\phi}$ so that Eq. (A 2) reduces to:

$$\overline{P_c} = (\overline{p_f} - p_o)\phi + \frac{1}{2}\phi^3. \tag{A 3}$$

If the outer pressure is larger than the fluid pressure, i.e., $p_o > p_f$, wall blowing (positive ϕ) causes negative contribution to P_c as shown in the first term of Eq. (A 3). This indicates that the fluid in the outer system can be introduced into the inner system without additional work due to the pressure difference between the inner and outer systems. A similar discussion can also be applied to wall suction when $p_o < p_f$. Meanwhile, we have to keep in mind that additional work is always required to maintain the pressure difference between the inner and outer systems. In high-speed transport applications, for example, the large dynamic pressure may be used for wall blowing. Even in such cases, utilization of air intake system may cause additional energy loss, and therefore deteriorate the total system efficiency.

In the case of zero-net-mass-flux blowing/suction, $\overline{\phi}$ is equal to zero by definition, so that Eq. (A 2) results in:

$$\overline{P_c} = \overline{p'_f \phi'} + \frac{1}{2}\overline{\phi'^3}. \tag{A 4}$$

It should be emphasized that $\overline{P_c}$ is independent of p_o and equal to the power received by the fluid system. The above definition of the control power input has been commonly used in previous studies, e.g., Iwamoto et al. (2002), Min et al. (2006) and Bewley (2009), and it is also employed in the present study as shown in Eq. (2.19).

In deriving Eq. (A 4), it is assumed that instantaneous negative P_c can compensate positive P_c at different time or location. Indeed, in the present study, P_c instantaneously shows a significant negative value, and consequently $\overline{P_c}$ defined by Eq. (A 4) mostly becomes negative. Since the energy recovery from the flow system is unrealistic, we can also introduce more conservative estimate of P_c so as to count only positive power input as:

$$\overline{P_c} = \overline{S_1 p'_f \phi'} + \frac{1}{2}\overline{S_2 \phi'^3}, \tag{A 5}$$

where S_1 and S_2 are switching coefficients defined as:

$$S_1 = \begin{cases} 1 & (p'_f \phi' > 0) \\ 0 & (p'_f \phi' < 0) \end{cases}, \quad S_2 = \begin{cases} 1 & (\phi' > 0) \\ 0 & (\phi' < 0) \end{cases}. \tag{A 6}$$

Alternatively, we can simply take absolute values as:

$$\overline{P_c} = \overline{|p'_f \phi'|} + \frac{1}{2}\overline{|\phi'|^3}. \tag{A 7}$$

This always gives more conservative estimate of $\overline{P_c}$ than Eq. (A 5). We confirmed that the present suboptimal and open-loop controls generally achieve $A_{net} > 1$ even when the conservative estimates (A 5, A 7) for P_c are used. It should be noted that, however, they are just reference values of P_c when the energy recovery from the flow system is not allowed.

We remark that the estimate (A 2) gives the lower limit of $\overline{P_c}$ based on the thermodynamic constraints, so that real power consumed by actuators should be much larger that the present estimate. Nonetheless, it is meaningful to introduce such ideal control power input in order to discuss the theoretical upper bound of control peformacne (see, e.g., Bewley (2009) and Fukagata et al. (2009)).

Appendix B. Cost function including analogy factor

Since the aim of the present study is to increase A above unity, it is straightforward to employ a cost function that explicitly includes A. For this purpose, one can define the following cost function instead of Eq. (3.17):

$$J = \frac{1}{S\Delta t}\int_S\int_t^{t+\Delta t}\frac{1}{2}(\phi_T^2+\phi_B^2)dtdS - \beta' A, \tag{B 1}$$

where β' is a relative merit of the dissimilarity to the control input. By taking into account Eq. (2.15), the Fréchet differential of J is obtained as follows:

$$\begin{aligned}\frac{\mathscr{D}J}{\mathscr{D}\phi}\tilde{\phi} &= \frac{1}{S\Delta t}\int_S\int_t^{t+\Delta t}\phi_B\tilde{\phi}_B+\phi_T\tilde{\phi}_T dtdS\\ &+\frac{\beta'}{C_f^2}\left\{2\mathrm{St}_m\frac{\mathscr{D}(C_f)}{\mathscr{D}\phi}\tilde{\phi}-C_f\frac{\mathscr{D}(2\mathrm{St}_m)}{\mathscr{D}\phi}\tilde{\phi}\right\}\\ &\approx \frac{1}{S\Delta t}\int_S\int_t^{t+\Delta t}\phi_B\tilde{\phi}_B+\phi_T\tilde{\phi}_T dtdS\\ &+\frac{2\beta'\mathrm{St}_m}{C_f^2 V\Delta t}\int_V\int_t^{t+\Delta t}y(q_1u_2'+u_1'q_2)dtdV\\ &-\frac{\beta'}{C_f V\Delta t}\int_V\int_t^{t+\Delta t}y(\eta u_2'+\theta' q_2)dtdV.\end{aligned} \tag{B 2}$$

Here, we employ the identities (2.13) and (2.14) in order to relate St_m and C_f with flow quantities. It should also be noted that Eqs. (2.13) and (2.14) hold in a fully developed sate, while the time integral in Eq. (B 2) is applied over a short-time interval Δt, since the suboptimal control theory takes into account short-time dynamics only. Hence, the approximate equality in Eq. (B 2) is deployed. It is found that Eq. (B 2) has the same form as Eq. (3.18). Therefore, the cost function defined in Eq. (3.17) can be considered as a more general form for dissimilar control. When Eq. (B 1) is employed as a cost function, the ratio of β and γ in Eq. (3.17) is equal to A as shown in Eq. (B 2). This indicates that the present cost function (3.17) with $\beta/\gamma = 1.0$ is equivalent to Eq. (B 1) when the amplitude of the control input is relatively small so that A remains close to unity.

In order to clarify how the different cost functions influence the control performance, the control results at the large control input of $\phi_{rms} = 0.05$ are summarized in Table 6. When the cost function (B 1) is used, C_f becomes less than that of uncontrolled flow, while St is more enhanced. This is because the cost function (B 1) results in larger weight for drag reduction than heat transfer enhancement, i.e., $\beta/\gamma > 1$, when $A > 1$ (see, Eq. (B 2)). Although the simultaneous enhancement of drag reduction and heat transfer is of great interest, the resultant A obtained by the cost function (B 1) is smaller than that obtain by the cost function (3.17) with $\beta/\gamma = 1.0$. Since our focus is on achievement of large A, we employ the cost function (3.17) with $\beta/\gamma = 1.0$ throughout this study.

Appendix C. Control applied on a single wall

The control inputs at the top and bottom walls optimized in the present study are always almost symmetric. Here, we briefly report results when the control is applied only to the bottom wall. In general, a similar traveling wave-like control input is obtained even in this case. In Fig. 24, the conditionally-averaged control inputs are compared in the two cases where the controls are applied on single and both walls. They agree fairly well. In Table 7, the control results are also listed. Generally, the control effects commonly decrease by half when the control is applied to a single wall only, while the fundamental

TABLE 6. Effect of cost function on control results at $\phi_{rms} = 0.05$.

	$C_f \cdot 10^2$	$\mathrm{St}_m \cdot 10^2$	A	A_{net}
no control	0.858	0.430	1.00	–
control with Eq. (3.17) and $\beta/\gamma = 1.0$	1.74	1.31	1.51	1.61
control with Eq. (B 1)	0.811	0.562	1.39	1.30

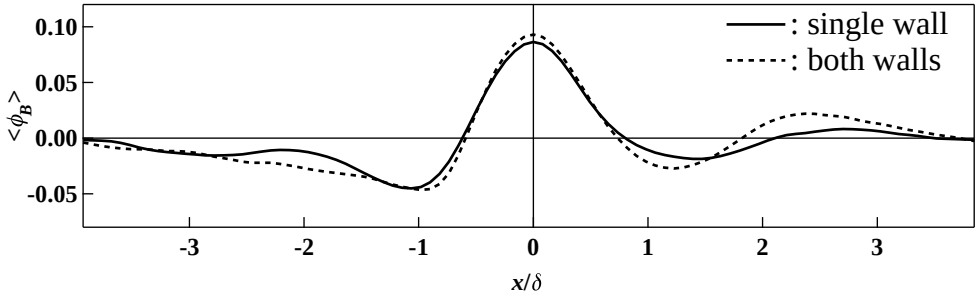

FIGURE 24. Conditionally-averaged control input $\langle\phi\rangle$ at the bottom wall for controls applied on single and both walls at $\phi_{\mathrm{rms}} = 0.05$.

TABLE 7. Control results for controls applied to single and both walls.

	$C_f \cdot 10^2$	$\mathrm{St}_m \cdot 10^2$	A	A_{net}	U_p	$\langle\phi\rangle_{\mathrm{rms}}/\phi_{\mathrm{rms}}$
no control	0.858	0.430	1.00	–	–	–
control applied on both walls	1.74	1.31	1.51	1.61	0.277	0.657
control applied on a single wall	1.32	0.850	1.29	1.31	0.269	0.576

properties of the traveling wave-like control input remain similar. These results imply that the control effect on one wall does not influence much that on the other wall.

REFERENCES

Antonia, R. A. & Krishnamoorthy, L. V. 1988 Correlation between the longitudinal velocity fluctuation and temperature fluctuation in the near-wall region of a turbulent boundary layer. *Int. J. Heat Mass Transfer* **31**, 723–730.

Bewley, T. 2009 A fundamental limit on the balance of power in a transpiration-controlled channel flow. *J. Fluid Mech.* **558**, 309–318.

Bewley, T., Moin, P. & Temam, R. 2001 DNS-based predictive control of turbulence: an optimal benchmark for feedback algorithms. *J. Fluid Mech.* **447**, 179–225.

Chilton, T. H. & Colburn, A. P. 1934 Mass-transfer coefficients, prediction from data on heat transfer and fluid friction. *Ind. Engng Chem.* **26**, 1183–1187.

Choi, H., Moin, P. & Kim, J. 1994 Active turbulence control for drag reduction in wall-bounded flows. *J. Fluid Mech.* **262**, 75–110.

Fukagata, K., Iwamoto, K. & Kasagi, N. 2002 Contribution of Reynolds stress distribution to the skin friction in wall-bounded flows. *Phys. Fluids* **14**, L73–L76.

Fukagata, K. & Kasagi, N. 2004 Suboptimal control of drag reduction via suppression of near-wall Reynolds shear stress. *Int. J. Heat Fluid Flow* **25**, 341–350.

Fukagata, K., Sugiyama, K. & Kasagi, N. 2009 On the lower bound of net driving power in controlled duct flows. *Physica D.* **238**, 1082–1086.

Iwamoto, K., Suzuki, Y. & Kasagi, N. 2002 Reynolds number effect on wall turbulence: toward effective feedback control. *Int. J. Heat Fluid Flow* **23**, 678–689.

Kasagi, N., Hasegawa, Y., Fukagata, K. & Iwamoto, K. 2010 Control of turbulent transport: Less friction and more heat transfer. *Trans. ASME* J:*J. Heat Transfer* **111**, in press.

Kasagi, N., Kuroda, A. & Hirata, M. 1989 Numerical investigation of near-wall turbulent heat transfer taking into account the unsteady heat conduction in the solid wall. *Trans. ASME* J:*J. Heat Transfer* **111**, 385–392.

Kasagi, N., Suzuki, Y. & Fukagata, K. 2009 Microelectromechanical systems-based feedback control of turbulence for skin friction reduction. *Annu. Rev. Fluid Mech.* **41**, 231–251.

Kasagi, N., Tomita, Y. & Kuroda, A. 1992 Direct numerical simulation of passive scalar field in a two dimensional turbulent channel flow. *Trans. ASME* J:*J. Heat Transfer* **114**, 598–606.

Keys, W., Crawford, M. E. & Weigand, B. 2005 Convective Heat and Mass Transfer, Fourth Edition. McGraw-Hill.

Kong, H., Choi, H. & Lee, S. L. 2001 Dissimilarity between the velocity and temperature fields in a perturbed turbulent thermal boundary layer. *Phys. Fluids* **13**, 1466–1479.

Lee, C., Kim, J. & Choi, H. 1998 Suboptimal control of turbulent channel flow for drag reduction. *J. Fluid Mech.* **358**, 245–258.

Lim, J. & Kim, J. 2004 A singular value analysis of boundary layer control. *Phys. Fluids* **16**, 1980–1988.

Mamori, H., Fukagata, K. & Hoepffner, J. 2010 The phase relationship in laminar channel flow controlled by travelling wave-like blowing or suction. *Phys. Rev. E* **81**, Art. 046304.

Min, T., Kang, S. M., Speyer J. L. & Kim, J. 2006 Sustained sub-laminar drag in a fully developed channel flow. *J. Fluid Mech.* **558**, 309–318.

Quadrio, M., Ricco, P. & Viotti, C. 2009 Streamwise-travelling waves of spanwise wall velocity for turbulent drag reduction. *J. Fluid Mech.* **627**, 161–178.

Reynolds, O. 1874 On the extent and action of the heating surface of steam boilers. In *Manchester Proc. Litl Phil. Soc.* **14**, 7–12.

Suzuki, H., Suzuki, K. & Sato, T. 1988 Dissimilarity between heat and momentum transfer in a turbulent boundary layer disturbed by a cylinder. *Int. J. Heat Mass Transfer* **31**, 259–265.

Yokoo, M., Kasagi, N. & Suzuki, Y. 2000 Optimal control of heat transfer and skin friction in wall turbulence. In *Proc. 3rd Int. Symp. Turbulence, Heat and Mass Transfer*, 949–956.